



Small rock-slope failures conditioned by Holocene permafrost degradation

DOI:

[10.1111/bor.12336](https://doi.org/10.1111/bor.12336)

Document Version

Accepted author manuscript

[Link to publication record in Manchester Research Explorer](#)

Citation for published version (APA):

Matthews, J. A., Winkler, S., Wilson, P., Tomkins, M. D., Dortch, J. M., Mourné, R. W., Hill, J. L., Owen, G., & Vater, A. E. (2018). Small rock-slope failures conditioned by Holocene permafrost degradation: a new approach and conceptual model based on Schmidt-hammer exposure-age dating, Jotunheimen, southern Norway. *Boreas*, 47(4), 1144-1169. <https://doi.org/10.1111/bor.12336>

Published in:

Boreas

Citing this paper

Please note that where the full-text provided on Manchester Research Explorer is the Author Accepted Manuscript or Proof version this may differ from the final Published version. If citing, it is advised that you check and use the publisher's definitive version.

General rights

Copyright and moral rights for the publications made accessible in the Research Explorer are retained by the authors and/or other copyright owners and it is a condition of accessing publications that users recognise and abide by the legal requirements associated with these rights.

Takedown policy

If you believe that this document breaches copyright please refer to the University of Manchester's Takedown Procedures [<http://man.ac.uk/04Y6Bo>] or contact uml.scholarlycommunications@manchester.ac.uk providing relevant details, so we can investigate your claim.



1
2
3 1 Small rock-slope failures conditioned by Holocene permafrost
4 2 degradation: a new approach and conceptual model based on Schmidt-
5 3 hammer exposure-age dating, Jotunheimen, southern Norway
6
7

8 JOHN A. MATTHEWS^{1*}, STEFAN WINKLER², PETER WILSON³, MATT D.
9 TOMKINS⁴, JASON M. DORTCH⁵, RICHARD W. MOURNE⁶, JENNIFER L.
10 HILL⁶, GERAINT OWEN¹ AND AMBER E. VATER¹
11

12 ¹ Department of Geography, College of Science, Swansea University, Singleton Park,
13 Swansea SA2 8PP, Wales, UK

14 ² Department of Geography and Geology, Julius-Maximilians-University Würzburg,
15 Am Hubland, 97070 Würzburg, Germany

16 ³ School of Geography and Environmental Sciences, Ulster University, Cromore
17 Road, Coleraine BT52 1SA, Northern Ireland, UK

18 ⁴ Cryosphere Research at Manchester, Department of Geography, University of
19 Manchester, Manchester M13 9PL, UK

20 ⁵ Kentucky Geological Survey, 228 Mining and Mineral Resources Building,
21 University of Kentucky, Lexington, Kentucky 40506, USA

22 ⁶ Department of Geography and Environmental Management, University of the West
23 of England, Coldharbour Lane, Bristol BS16 1QY, UK
24
25

26 * corresponding author: J.A.Matthews@Swansea.ac.uk
27
28

29 Rock-slope failures (RSFs) constitute significant natural hazards but the geophysical
30 processes which control their timing are poorly understood. However, robust
31 chronologies can provide valuable information on the environmental controls on RSF
32 occurrence: information which can inform models of RSF activity in response to
33 climatic forcing. This paper uses Schmidt-hammer exposure-age dating (SHD) of
34 boulder deposits to construct a detailed regional Holocene chronology of the
35 frequency and magnitude of small rock-slope failures (SRSFs) in Jotunheimen,
36 Norway. By focusing on the depositional fans of SRSFs ($\leq 10^3 \text{ m}^3$), rather than on the
37 corresponding features of massive RSFs ($\sim 10^8 \text{ m}^3$), 92 single-event RSFs are targeted
38 for chronology building. A weighted SHD age-frequency distribution and probability
39 density function analysis indicate four centennial- to millennial-scale periods of
40 enhanced SRSF frequency, with a dominant mode at $\sim 4.5 \text{ ka}$. Using change detection
41 and discreet Meyer wavelet analysis, in combination with existing permafrost depth
42 models, we propose that enhanced SRSF activity was primarily controlled by
43 permafrost degradation. Long-term relative change in permafrost depth provides a
44 compelling explanation for the high-magnitude departures from the SRSF background
45 rate and accounts for (1) the timing of peak SRSF frequency, (2) the significant lag
46 ($\sim 2.2 \text{ ka}$) between the Holocene Thermal Maximum and the SRSF frequency peak
47 and (3) the marked decline in frequency in the late-Holocene. This interpretation is
48 supported by geomorphological evidence, as the spatial distribution of SRSFs is
49 strongly correlated with the aspect-dependent lower altitudinal limit of mountain
50 permafrost in cliff faces. Results are indicative of a causal relationship between
51 episodes of relatively warm climate, permafrost degradation and the transition to a
52 seasonal-freezing climatic regime. This study highlights permafrost degradation as a
53 conditioning factor for cliff collapse, and hence the importance of paraperiglacial
54 processes; a result with implications for slope instability in glacial and periglacial
55 environments under global warming scenarios.
56
57
58
59
60

1
2
3 51
4 52
5 53 *Key words:* small rock-slope failures (SRSFs), Schmidt-hammer exposure-age dating
6 54 (SHD), permafrost degradation, Holocene Thermal Maximum, climate-change
7 55 impacts, paraperiglacial processes, southern Norway
8 56
9 57

10 58 Rock-slope failures (RSFs) are indicative of instability in the landscape and reflect
11 59 several geophysical processes and potential trigger factors related to rock mechanics,
12 60 geomorphology, hydrology and environmental change. Moreover, RSFs constitute
13 61 significant natural hazards. As a result, understanding the environmental controls on
14 62 RSF occurrence provides crucial information which can inform modelling of future
15 63 RSF activity in response to climate forcing (Rapp 1960a, 1960b; Brunsten & Prior
16 64 1984; Evans et al. 2006; Clague & Stead 2012; Davies 2015).
17 65

18 66 Numerous RSFs have been investigated in regions of high relief and, in some
19 67 cases, RSF deposits have been dated (e.g. Korup et al. 2007; Ballantyne et al. 2014a,
20 68 2014b). However, previous research has primarily focused on modern examples,
21 69 spectacular cases or small numbers of massive rock-slope failures (MRSFs; $\sim 10^8$ m³)
22 70 which, in combination with uncertainty associated with current geochronological
23 71 approaches, limits our understanding of the fundamental geophysical processes and
24 72 environmental controls that determine RSF occurrence. Particular studies of RSFs
25 73 have used a variety of techniques and, on some occasions, a combination of
26 74 geochronological methods (Lang et al. 1999; Hermanns et al. 2000; Crosta & Clague
27 75 2009; Deline & Kirkbride 2009; Prager et al. 2009; Pánek 2014; Böhme et al. 2015;
28 76 Moreiras et al. 2015; Mercier et al. 2017), but the opportunities for accurate dating are
29 77 relatively rare.
30 78

31 79 The primary method for numerical-age dating of RSF deposits is terrestrial
32 80 cosmogenic nuclide dating (TCND; ¹⁰Be, ²⁶Al, ³⁶Cl) as this technique permits direct
33 81 sampling and age determination of the exposed rock surfaces associated with RSFs
34 82 (Hermanns et al. 2001, 2004, 2017; Cossart et al. 2008; Dortch et al. 2009; Ivy-Ochs
35 83 et al. 2009; Penna et al. 2011; Ballantyne & Stone 2013; Ballantyne et al. 2013,
36 84 2014a, 2014b; Böhme et al. 2015; Schleier et al. 2015, 2017). However, the high
37 85 financial cost of this technique limits its routine application which, in turn, often
38 86 prevents statistically robust identification and rejection of erroneous results (Tomkins
39 87 et al. 2018b). Consequently, there are still few reliable chronologies of RSFs which
40 88 limits our understanding of the environmental factors determining their spatial and
41 89 temporal occurrence.
42 90

43 91 In this paper we develop a methodology for the investigation and dating of
44 92 RSFs, with targeted study of ‘small rock-slope failures’ (SRSFs; $< 10^3$ m³). This focus
45 93 has the advantage over MRSFs of permitting the dating and study of a relatively large
46 94 sample of simple, likely single-event RSFs within a specified region. The
47 95 methodology has been developed in conjunction with the relatively new calibrated-
48 96 age dating technique of Schmidt-hammer exposure-age dating (SHD) (Shakesby et al.
49 97 2006, 2011; Matthews & Owen 2011; Matthews et al. 2015; Matthews & Wilson
50 98 2015; Winkler et al. 2010, 2016; Wilson et al. 2017). SHD has the potential to
51 99 estimate the numerical age of rock-surface exposure at low cost with comparable
52 100 accuracy and precision, and greater representativeness, than TCND over the Late
53
54
55
56
57
58
59
60

1
2
3 101 Glacial and Holocene (cf. Winkler 2009; Winkler & Matthews 2010; Matthews &
4 102 Winkler 2011; Matthews et al. 2013; Wilson & Matthews 2016; Tomkins et al. 2016,
5 103 2018a, 2018b, 2018c).

6 104
7 105 Specific objectives of this paper are three-fold:

- 8 106
9 107
 - 10 108 • To establish a Holocene chronology of SRSF events in the alpine zone of
 - 11 109 Jotunheimen, southern Norway and identify any phases of instability;
 - 12 110 • To explore relationships between the timing of Holocene SRSF events and
 - 13 111 regional environmental changes, including climatic changes; and
 - 14 112 • To develop further the potential of SHD as a calibrated-age dating technique
 - 15 113 in the context of RSFs.

16 114

17 115 Study area and environmental context

18 116

19 117 SRSFs were investigated in a broad area of northern Jotunheimen, the highest
20 118 mountain massif in southern Norway, which culminates in Galdhøpiggen (2469 m
21 119 above sea level; a.s.l.). The study area extends from Sognefjell in the west to
22 120 Veodalen in the east (Fig. 1). Most SRSFs were found in Leirdalen, Bjørndalen (a
23 121 western tributary valley to upper Leirdalen) and Gravdalen. The SRSFs occurred over
24 122 an altitudinal range of 600 m (950-1550 m a.s.l.), mainly above the tree line, which
25 123 lies at ~1000-1100 m a.s.l., in the alpine zone, and mainly in the low- and mid-alpine
26 124 belts (Moen 1999). Examples of SRSFs from the study area are shown in Fig. 2.

27 125
28 126 Climatic data from the Sognefjell meteorological station (1413 m a.s.l.)
29 127 indicate a mean annual air temperature of +3.1 °C (mean July temperature +13.4 °C;
30 128 mean January temperature -10.7 °C), and a mean annual precipitation of 860 mm,
31 129 much of which occurs as snow (climatic normals AD 1961-1990; Aune 1993; Førland
32 130 1993). These data are consistent with a lower altitudinal limit of discontinuous
33 131 permafrost at ~ 1450 m a.s.l. in the Galdhøpiggen massif (Ødgård et al. 1992; Isaksen
34 132 et al. 2002; Farbrot et al. 2009; Lilleøren et al. 2012) with permafrost limits rising
35 133 eastwards as continentality increases (Etzelmüller et al. 2003; Ginås et al. 2017).
36 134 However, Hipp et al. (2014) have demonstrated a large difference of several hundred
37 135 metres in the lower limits of permafrost between north- and south-facing rock walls.
38 136 In the Galdhøpiggen massif, the lower altitudinal limit of rock-wall permafrost is
39 137 located at 1500-1700 m a.s.l. in south-facing rock walls but only 1200-1300 m a.s.l. in
40 138 shaded, north-facing rock walls (Hipp et al. 2014). Small valley glaciers, cirque
41 139 glaciers and ice caps are common at and above these altitudes on the surrounding
42 140 mountain peaks and plateaux (Andreassen & Winsvold 2012).

43 141
44 142 The metamorphic geology of the region consists primarily of pyroxene-
45 143 granulite gneiss with peridotite intrusions and quartzitic veins (Battey & McRitchie
46 144 1973, 1975; Lutro & Tveten 1996), and gabbroic gneiss in the area investigated on
47 145 Sognefjell (Gibbs & Banham 1979). Only boulders and bedrock of pyroxene-
48 146 granulite gneiss and gabbroic gneiss were used in this study, as described below.
49 147 Although these broad lithological categories include quite variable mineralogy, any
50 148 differences in surface R-values due to lithology will likely be significantly smaller
51 149 than the effect of variable exposure age given the relatively long Holocene
52 150 timescales of exposure and limited climatic variability within the study region.

1
2
3 151 Topographically, most of the valley-side slopes have experienced a considerable
4 152 degree of glacial erosion, although elements of ancient palaeic surfaces are
5 153 preserved in the landscape (Ahlmann 1922; Gjessing 1967; Lidmar-Bergström et al.
6 154 2000) due, at least in part, to non-erosive, cold-based conditions during glaciations.
7
8 155

9 156 Jotunheimen was located near the position of the main ice-divide and ice-
10 157 accumulation area of the Scandinavian ice-sheet at the maximum of the Last
11 158 (Weichselian) Glaciation. Deglaciation of the main valleys is likely to have occurred
12 159 by ~9.7 ka, following the Erdalen Event, late in the Preboreal chronozone (Dahl et
13 160 al. 2002; Matthews & Dresser 2008; Velle et al. 2010). Most glaciers appear to have
14 161 melted away during the Holocene Thermal Maximum (Nesje 2009) when permafrost
15 162 limits were also higher than today (Lilleøren et al. 2012), but regenerated during
16 163 neoglaciation, certainly by 5.5 ka and possibly as early as 7.6 ka (Ødgård et al.
17 164 2017). Both neoglaciation and lowering of permafrost limits occurred as a result of
18 165 climatic deterioration (cooler and wetter) in the late Holocene, culminating in the
19 166 Little Ice Age glacier maximum of the eighteenth century (Matthews 1991, 2005;
20 167 Matthews & Dresser 2008). Future predicted mean annual warming of 0.3-0.4 °C
21 168 per decade in Scandinavia (Benestad 2005) is likely to lead to unprecedented glacier
22 169 retreat (Nesje et al. 2008) and a continuing rise in permafrost limits (Lilleøren et al.
23 170 2012).
24 171

25 171

26 172

27 173 Methodology

28 174

29 175 *Definitions and criteria for recognition of SRSFs*

30 176

31 177 The term ‘rock-slope failure’ (RSF) refers to both (1) a mass-movement process
32 178 involving the deformation and loss of integrity of a volume of intact bedrock followed
33 179 by its *en masse* collapse and downslope movement under gravity and (2) the resulting
34 180 landform. This definition is used here to distinguish RSF from ‘rockfall’ – the
35 181 smaller-scale process involving the piecemeal detachment and free fall of individual
36 182 rock particles – even though the term rockfall is commonly used at all scales,
37 183 including the largest landslides and rock avalanches (MRSFs), which are often
38 184 complex and multiphase (cf. Bates & Jackson 1987; Cruden & Varnes 1996; Braathen
39 185 et al. 2004; Luckman 2004; Evans et al. 2006; Hermanns et al. 2006; Jarman 2006;
40 186 Frattini et al. 2012; Hermanns & Longva 2012; Shakesby 2014; Brideau & Roberts
41 187 2015).
42 188

43 188

44 189 Fundamental to this study was the selection of SRSF landforms that
45 190 represented, as far as it was possible to ascertain, the product of single events. Criteria
46 191 for recognition of such SRSFs were as follows:
47 192

48 192

- 49 193
- 50 194 • a compact and coherent depositional fan of predominantly angular boulders
51 195 located close to a bedrock cliff.
 - 52 196 • a simple erosional scar in the cliff, immediately upslope of the fan, which is
53 197 comparable in scale to the fan and therefore represents the likely source of the
54 198 failed rock material;
 - 55 199 • an absence of alternative sources of boulders up-slope of the scar.

56 199

57 199

58 199

59 199

60 199

1
2
3 200 Although no upper limit was placed on the size of the SRSFs recognized in this study,
4 201 these criteria become less easily satisfied as RSFs increase in size. The lower size
5 202 limit was the practical one of sufficient boulders for reliable Schmidt hammer
6 203 measurement. Thus, the size range included in the study was determined by the RSFs
7 204 in the region. Furthermore, the 92 investigated cases represent the whole population
8 205 of SRSFs that satisfied the above criteria in the study area.
9 206

10 207 *Measurement of SRSF characteristics*

11 208
12 209 Estimates were made in the field of the length and average width of the depositional
13 210 fan of each SRSF. Aspect and the altitude of the fan apex were estimated from
14 211 topographic maps at a scale of 1:50,000 with a contour interval of 20 m,
15 212 supplemented by altimeter and GPS measurements in the field. Fan volume was
16 213 calculated from the length and average width measurements, assuming an average fan
17 214 thickness of 1 m and a voids fraction (volume of voids/total fan volume) of 40%.
18 215 Although some of the largest fans are thicker than 1 m in places, all are thinly spread
19 216 across and down slope and rarely involve piles of debris. Lower voids fractions have
20 217 generally been used for MRSFs, rock avalanches, talus and other mass movement
21 218 types involving mixed particle sizes, fine matrix and/or compacted material (Owen et
22 219 al. 2010; Sass & Wollny 2001; Hungr & Evans 2004; Wilson 2009; Stock &
23 220 Uhrhammer 2010; Sandøy et al. 2017). The value of 40% is justified given the
24 221 absence of fine matrix (Fig. 2) and lack of compaction, and its compatibility with
25 222 similar values for clean, open-graded, angular aggregate material used as backfill in
26 223 foundation engineering (StormTech 2012; cf. Dann et al. 2009).
27 224

28 225 *Measurement of Schmidt-hammer R-values*

29 226
30 227 N-type mechanical Schmidt hammers (Proceq 2004; Winkler & Matthews 2014) were
31 228 used to measure rebound (R-) values from 100 boulders in each depositional fan. R-
32 229 values reflect lithologically-determined rock hardness and the compressive strength of
33 230 the rock surface: hence, R-values decline following exposure of a rock surface to
34 231 subaerial weathering. For boulder surfaces of the same lithology but differing age, R-
35 232 values therefore reflect the exposure age (time elapsed since exposure) of the rock
36 233 surface. Use of one impact per boulder from a large sample of boulders ensures that
37 234 the R-value frequency distribution can be used to approximate the boulder-age
38 235 distribution (Matthews et al. 2014, 2015).
39 236

40 237 Precautions taken to eliminate or reduce possible sources of uncertainties and
41 238 errors in Schmidt-hammer measurement included avoiding unstable or small boulders,
42 239 boulder or bedrock edges, joints or cracks, unusual lithologies and lichen-covered or
43 240 wet surfaces (cf. Shakesby et al. 2006; Matthews & Owen 2010; Viles et al. 2011).
44 241 Rock surfaces were not cleaned or artificially abraded prior to impact with the
45 242 Schmidt hammer (cf. the carborundum treatment of Viles et al. 2011) because such
46 243 treatment would likely remove age-related weathering effects. However, there is
47 244 continued debate as to whether rock surfaces should be abraded prior to testing
48 245 (Moses et al. 2014) although a consistent sampling approach may enable age-related
49 246 information to be retained (c.f. Tomkins et al. 2018b). Where possible, horizontal
50 247 boulder surfaces were impacted but only vertical rock faces were available on cliffs.
51 248 The two hammers used had been recently re-calibrated at a recognised service centre
52 249 and were tested frequently on the manufacturer's test anvil throughout the study to
53
54
55
56
57
58
59
60

1
2
3 250 ensure there had been no deterioration in instrument performance following large
4 251 numbers of impacts (cf. McCarroll 1987, 1994; Winkler & Matthews 2016).
5 252 Measurements at 84 sites were restricted to rock surfaces of pyroxene-granulite
6 253 gneiss. At the 8 sites on Sognefjell, gneissic rocks with gabbroic textures were used,
7 254 which necessitated a separate calibration equation (see below).
8 255

9 256 *Testing the validity of the approach*
10 257

11 258 In order to test the validity of our approach, and especially whether the boulders
12 259 comprising the depositional fans actually represent single rock-failure events and
13 260 whether the local source of the boulders had been correctly identified, R-value
14 261 distributions associated with six fans and their corresponding scars were investigated.
15 262 Two separate tests of validity were conducted.
16 263

17 264 First, in the *fan-scar comparison test*, a comparable sample of R-values ($n =$
18 265 100) from the surface of the corresponding scar was compared with the R-value
19 266 distribution of the fan to identify whether or not the scar was the likely source of the
20 267 boulders in the fan. If the scar was indeed the source of the boulders, the expectation
21 268 would be no significant difference in the R-values derived from the scar and its
22 269 corresponding fan because both would have experienced exposure over the same
23 270 period of time.
24 271

25 272 Second, the *unfailed-cliff test* required a comparable sample of R-values ($n =$
26 273 100) from the adjacent intact (unfailed) bedrock cliff and also aimed to establish that
27 274 the cliff was the bedrock source for the fan boulders. If this was the case, it would be
28 275 expected that R-values from the unfailed cliff would be similar to or lower than the R-
29 276 values of both the scar and the fan. Any departure from these expectations would
30 277 indicate possible flaws in our approach.
31 278

32 279 The principles behind the fan-scar comparison test and the unfailed-cliff test
33 280 are illustrated in Fig. 3, which also shows the expected relationships between R-
34 281 values from the fans and R-values from the rock surfaces used as control points in the
35 282 calibration equations.
36 283

37 284 *Calibrated-age dating using SHD*
38 285

39 286 Although there was earlier use of the Schmidt hammer for dating purposes (e.g.
40 287 Matthews & Shakesby 1984; Nesje et al. 1994; Aa & Sjøstad 2000; Aa et al. 2007),
41 288 SHD has been developed more recently as a calibrated-age dating technique (Colman
42 289 et al., 1987) incorporating measures of uncertainty based on statistical confidence
43 290 intervals (cf. Shakesby et al. 2006; Matthews & Owen 2011; Matthews & Winkler
44 291 2011; Matthews & McEwen 2013). Critically, this involves the derivation of a
45 292 calibration equation and confidence limits for age.
46 293

47 294 The calibration equation is based on linear regression of surface age (Y) on
48 295 mean R-value (X):
49 296

50 297
$$Y = a + bX \quad (1)$$

51 298

1
2
3 299 A linear relationship can be justified on both theoretical and empirical grounds.
4 300 Although chemical weathering rates are likely to decline over longer timescales
5 301 (Colman 1981; Colman & Dethier 1986; Stahl et al. 2013; Tomkins et al. 2018a,
6 302 2018b), near-linear rates can be expected over the Holocene timescale, especially
7 303 where relatively resistant lithologies are subject to relatively slow rates of chemical
8 304 weathering in a periglacial environment (André 1996, 2002; Nicholson 2008, 2009;
9 305 Matthews & Owen 2011; Matthews et al. 2016). Although physical (freeze-thaw)
10 306 weathering is well known in periglacial environments, it is highly dependent on
11 307 moisture availability for ice-lens growth (Hallet et al. 1991; Hall et al. 2002; Murton
12 308 et al. 2006; Matsuoka & Murton 2008) and there is no evidence that it has affected the
13 309 well-drained surfaces used in this study (neither boulders in the dated depositional
14 310 fans nor bedrock control surfaces).
15 311

16 312 Furthermore, Shakesby et al. (2011) specifically tested the linearity
17 313 assumption in relation to granite boulders on independently-dated staircases of raised
18 314 beaches deposited since 10.4 ka in northern Sweden, with the conclusion that the
19 315 relationship between mean R-value and age was best described by a linear function.
20 316 The same conclusion can be reached from age-calibration curves in the British Isles
21 317 (Tomkins et al. 2018a) and the Pyrenees (Tomkins et al. 2018b), which are based on
22 318 54 and 52 ¹⁰Be TCND-dated granitic surfaces respectively, all associated with glacial
23 319 depositional or erosional landforms (moraine boulders or ice-sculpted bedrock).
24 320 While the Pyrenean age-calibration curve is clearly non-linear over the full age range
25 321 of ~50 ka, both age-calibration curves evidence linearity over the last ~20 ka. Other
26 322 studies that have suggested non-linear relationships have involved long timescales
27 323 and/or have had insufficient control points to test the linearity assumption rigorously
28 324 over the Holocene timescale (e.g. Betts & Latta 2000; Sánchez et al. 2009; Černá &
29 325 Engel 2011; Stahl et al. 2013).
30 326

31 327 Based on two control points, the *b* coefficient can be defined as:
32 328

$$33 329 \quad b = (y_1 - y_2) / (x_1 - x_2) \quad (2)$$

34 330
35 331 where x_1 and x_2 are the mean R-values of the older and younger control points,
36 332 respectively, and y_1 and y_2 are their respective ages. Once the *b* coefficient is known,
37 333 the *a* coefficient is found by substitution in equation (1). Only two control points of
38 334 widely differing age are available from Jotunheimen (see below). Provided they are of
39 335 good quality, however, two control points are sufficient for accurate R-value
40 336 calibration provided the underlying relationship between R-value and age is
41 337 approximately linear.
42 338

43 339 For a landform produced by a single event, the SHD age resulting from this
44 340 calibration is the average age of the surface boulders and hence the landform age
45 341 (Matthews et al. 2015). Confidence intervals for the SHD age (95%) are calculated as
46 342 the total error (C_t) by combining the error associated with the calibration equation (C_c)
47 343 with the sampling error associated with the surface to be dated (C_s):
48 344

$$49 345 \quad C_t = \sqrt{(C_c^2 + C_s^2)} \quad (3)$$

$$50 346 \quad C_c = C_o - [(C_o - C_y) (R_s - R_o) / (R_y - R_o)] \quad (4)$$

$$C_s = b[ts / \sqrt{(n-1)}] \quad (5)$$

where C_o and C_y are the 95% confidence intervals of the older and younger control points (in years); and R_o , R_y and R_s are the mean R-values of the older control point, the younger control point and the surface to be dated, respectively. C_s depends on the number of R-value impacts on the surface to be dated (sample size, n), the standard deviation of those impacts (s), and Student's t statistic. Thus, the confidence interval (C_i) associated with any SHD age depends not only on the sample sizes used to establish the calibration equation and characterize the surface to be dated but also the natural variability exhibited by all the rock surfaces involved.

Control points for calibration equations

For this study, we constructed separate calibration equations for rock surfaces composed of pyroxene-granulite gneiss and gabbroic gneiss (each equation based on two control points). Data for the older control points, which relate to glacially-scoured bedrock surfaces, were taken from Matthews & Owen (2010). Their data from four sites in Leirdalen and Gravdalen (S and E Smørstabbtindan) were used for the pyroxene-granulite gneiss calibration equation: four sites near Leirbreen and Bøverbreen, close to Sognefjell (W Smørstabbtindan) supplied the data for the gabbroic gneiss calibration equation (Fig. 1).

Evidence for deglaciation of these sites is provided by basal ^{14}C dates from peat bogs and lakes in Leirdalen, Bjørndalen, and on Sognefjell (Table 2). These ^{14}C dates were recalibrated to calendar age ranges with the OxCal online program (v.4.3) using the IntCal13 calibration dataset (Reimer et al. 2013). Although one of the calibrated age ranges is significantly older, 9.7 ka is the only date for deglaciation that is compatible with the other four ^{14}C dates. Use of 9.7 ka as the age of the old control points for SHD calibration can be justified on the further grounds that it is the expected date for termination of the Erdalen Event in neighbouring regions (Dahl et al. 2002) and is consistent with empirical evidence for and large-scale modeling of deglaciation in southern Norway (Dahl et al. 2002; Goehring et al. 2008; Nesje 2009; Mangerud et al. 2011; Hughes et al. 2016; Stroeven et al. 2016). Thus, the potential errors in the old control points appear to be small in relation to the calibration errors (C_o and C_s) that are taken fully into account in this study.

Calibration equations given in Matthews & Owen (2010) for these rock types could not be used because their younger control points were derived from glacially-abraded surfaces from glacier forelands. Such smooth surfaces are not appropriate as a source of young control points for dating the exposure-age of boulders originating from SRSFs, which are rougher in texture yielding lower R-values than abraded surfaces of the same age (Shakesby et al. 2006; Matthews & McEwen 2013; Matthews et al. 2015). In contrast, after prolonged weathering, originally smooth surfaces are expected to yield similar R-values, and hence SHD ages, to initially rough surfaces.

Young control points with similar roughness properties to fresh boulder surfaces derived from SRSFs were therefore sought. These included: (1) boulders and bedrock surfaces produced by a recent rock-slope failure in Gravdalen and (2) bedrock exposed recently in road cuts in Gravdalen and on Sognefjell (Fig. 1). Both types of surfaces have been shown in previous studies to yield R-values that are

1
2
3 399 statistically indistinguishable from each other provided sufficient care is taken to
4 400 impact only truly fresh rock surfaces (Matthews & Wilson 2015; Matthews et al.
5 401 2016). Furthermore, both types of recent rock surfaces used as young control points in
6 402 this study were lichen-free and hence were assigned a maximum exposure age of 25
7 403 years based on various estimates of the time required for the establishment (ecesis) of
8 404 crustose lichens on bedrock surfaces in this environment (Matthews 2005; Matthews
9 405 & Owen 2008; Matthews & Vater 2015). Errors in the age of the young control point
10 406 are therefore considered to be negligible in the context of this study.
11 407

12 408 *Chronology construction and analysis*

13 409

14 410 Holocene chronologies of SRSF events were constructed from the SHD ages of the 92
15 411 SRSF fans using a number of statistical approaches. First, graphical analysis of age-
16 412 frequency distributions used 2000-yr, 1000-yr, 500-yr and 200-yr time intervals to
17 413 define major clusters of SHD ages and hence possible multi-centennial to millennial
18 414 phases of enhanced SRSF frequency (Matthews et al. 2009; Matthews & Seppälä
19 415 2015). Based on the same events weighted according to their rock volume, a second
20 416 chronology was constructed showing the changing magnitude of SRSF events through
21 417 the Holocene.
22 418

23 419 In order to take account of dating uncertainty, a weighted age-frequency
24 420 distribution was constructed in which each SHD age was plotted over five 200-yr age
25 421 classes: a weight of 4 was used for the central class; the second and fourth classes
26 422 were weighted 2. Thus, the SHD age was plotted over a range of 1000 yr, consistent
27 423 with the average 95% confidence interval of ± 991 yr calculated for the 92 SRSF fans
28 424 (see below). One-sample χ^2 tests were used to test the hypothesis that the dated events
29 425 were sampled from an underlying population of events with an even distribution
30 426 through time.
31 427

32 428 To support weighted age-frequency analysis, the distribution of calculated
33 429 SRSF ages was analysed using probability density function analysis. Probability
34 430 density estimates (PDEs) were produced and modelled to separate out individual
35 431 Gaussian distributions using the KS density kernel in MATLAB (2015) and a
36 432 dynamic smoothing window based on age uncertainty (cf. Dortch et al. 2013). The
37 433 sum of individual Gaussian distributions integrates to the cumulative PDE at 1000
38 434 iterations to obtain a good model fit. The goodness of fit between the re-integrated
39 435 PDE, which is derived from individual Gaussian distributions, and the cumulative
40 436 PDE, which is derived from the full age dataset, is indicated graphically. PDE
41 437 analysis was repeated using a number of individual Gaussian distributions ($n = 1-10$).
42 438 To avoid over-interpretation of SRSF modes, the PDE model with the minimum
43 439 number of individual Gaussian distributions, which also achieved a good model fit,
44 440 was selected. This analytical method has primarily been employed in studies using
45 441 ^{10}Be (cf. Dortch et al. 2013; Murari et al. 2014) or SHD (Barr et al. 2017; Tomkins et
46 442 al. 2018a; 2018b; 2018c) to account for negative or positive skew of moraine boulder
47 443 datasets and to identify and reject ages that are compromised by moraine degradation
48 444 (Briner et al. 2005; Heyman et al. 2011) or nuclide inheritance (Hallet & Putkonen
49 445 1996). In these applications, PDE analysis and interpretation of individual Gaussian
50 446 distributions (cf. Fig. 3 in Dortch et al. 2013) is based on the assumption that analysed
51 447 ages relate to a single event e.g. moraine deposition. This assumption is clearly not
52 448 applicable to the analysis of SRSF ages, as each numerical age relates to a distinct
53
54
55
56
57
58
59
60

1
2
3 449 event and an individual landform. As a result, individual Gaussian distributions are
4 450 interpreted as reflecting the temporal clustering of events. The characteristics of
5 451 individual Gaussian distributions, i.e. the peak probability density, width of PDE tails,
6 452 1σ uncertainties and the number of contributing ages (Fig. 7), were used to assess the
7 453 significance and temporal clustering of SRSF events in Jotunheimen over the last ~ 10
8 454 ka.
9 455

10 456 The individual distributions resulting from the PDE analysis indicated that
11 457 further analysis was necessary. Thus, a change detection analysis approach was
12 458 undertaken in MATLAB (2015) to identify statistically unique events. Change
13 459 detection analysis utilizes the cumulative sum algorithm (cusum), which is commonly
14 460 used to detect abrupt change in time series data in fields ranging from seismology
15 461 (Dera & Shumwayb 1999), remote sensed imagery (Lu et al. 2016), and GPS
16 462 monitoring (Goudarzi et al. 2013). Parameters were set by using the average
17 463 frequency and occurrence (~ 1 occurrence per 100 years) of SRSFs throughout the
18 464 Holocene to filter out ‘background’ SRSF occurrence. The alarm limit was set at ≥ 2
19 465 standard errors above background. To further explore the temporal pattern of SRSFs,
20 466 discrete Meyer wavelet analysis was undertaken in MATLAB (2015) to decompose
21 467 SRSF occurrence through time. Wavelets are discrete oscillations in both time and
22 468 amplitude and, as such, are useful for identifying discrete events. Wavelet analysis
23 469 has been used to identify climate signals from various records including δO^{18} (Lau &
24 470 Weng 1995), and sea surface temperature (Torrence & Compo 1998). The 100 yr
25 471 binned SRSF age data was passed through the discrete Meyer wavelet with six levels
26 472 of deconvolution.
27 473

28 474 Major and minor changes in SRSF activity were then compared with changes
29 475 in regional Holocene climatic and other geo-environmental indicators to infer possible
30 476 causes. Specific analyses were performed to investigate relationships between the
31 477 occurrence of SRSF events and the lower altitudinal limits of discontinuous
32 478 permafrost using aspect-dependent limits determined for rock walls in the
33 479 Galdhøpiggen massif by Hipp et al. (2014). The current (AD 2010-2013) lower limits
34 480 that were used for rock walls facing north, east, south and west were 1250 m, 1450 m,
35 481 1600 m and 1450 m, respectively.
36 482
37 483

38 484 Results

39 485 *Data on the SRSFs*

40 486
41 487
42 488 Data on the size and environmental characteristics of the SRSFs are summarized in
43 489 Table 1 and Fig. 4. The volume of the fans (Fig. 4A) ranges from 12 to 2520 m³, with
44 490 90% <1000 m³, 40% <100 m³ and a median size of only 180 m³. The altitudinal range
45 491 is 960 to 1550 m a.s.l. (Fig. 4B), with a mean altitude of 1340 m a.s.l. There is a
46 492 preferred aspect with 43% facing east, 34% facing south and 17% facing west, but
47 493 only 5% facing north (Fig. 4C).
48 494

49 495 Schmidt-hammer R-values vary widely between SRSFs (Table 1) and the
50 496 frequency distribution of mean R-values reveals several important features (Fig. 4D).
51 497 Mean R-values exhibit a very wide range of >20 units from 37.0 to 57.5. The overall
52 498 mean R-value across the 92 SRSFs is 48.2 but those R-values associated with
53
54
55
56
57
58
59
60

1
2
3 499 gabbroic gneiss (overall mean R-value 39.4, n = 8) are appreciably lower than the
4 500 remainder involving pyroxene-granulite gneiss (overall mean R-value 49.1, n = 84).
5 501 The latter value corresponds closely with the 49-50 modal class for the distribution.
6 502

7 503 *Control-point data and calibration equations*
8 504

9 505 Data from the control points (Table 3) indicate widely different mean R-values
10 506 (differing by at least 20 units) for surfaces that differ in age by ~9700 years. It should
11 507 also be noted that the overlapping 95% confidence intervals associated with each pair
12 508 of replicates for particular control points indicate that their mean R-values do not
13 509 differ significantly from each other. Control surfaces of the same age on different
14 510 lithologies are, however, characterized by non-overlapping confidence intervals, and
15 511 thus show significantly different mean R-values and justify the use of separate
16 512 calibration equations for SRSFs developed in pyroxene-granulite gneiss and gabbroic
17 513 gneiss. The calibration equations derived from these data for the two lithologies are
18 514 shown in Figure 5 alongside the linear relationships they represent.
19 515

20 516 *Fan-scar-cliff comparison tests*
21 517

22 518 Mean R-values for three of the six fans tested did not differ significantly from the
23 519 mean R-values of the corresponding scars, in accordance with expectation (Fig. 3 and
24 520 Table 4). However, three fans (Nos 51, 58 and 81) are characterized by mean R-
25 521 values that are significantly lower than the mean R-values from their scars. This
26 522 suggests one or more of four possible explanations: (1) rock surfaces of some
27 523 boulders in these fans are more weathered because they include the products of older
28 524 rock failures than those that produced the measured bedrock faces of the scars; (2)
29 525 some of the measured R-values from boulders in the fans reflect the incorporation of
30 526 bedrock surfaces that were pre-weathered on the cliff face before the failures
31 527 occurred; (3) some of the R-values from boulders in the fans reflect the incorporation
32 528 of inherited structures (e.g. joint planes) that were pre-weathered at depth before the
33 529 failures occurred; and (4) at least part of the cliff bedrock is more resistant to
34 530 weathering than the boulder surfaces measured in the fans. Interestingly, no fan
35 531 exhibits a mean R-value that is significantly greater than that of its corresponding
36 532 scar. This shows that even where more than one phase of activity seems possible, any
37 533 blocks that were later removed from the scars were insufficient in number to affect
38 534 appreciably the mean R-values of the fans.
39 535

40 536 Comparisons between scars and unfailed cliffs or between fans and unfailed
41 537 cliffs are entirely in agreement with expectation. In three cases (fan Nos 5, 51 and 58)
42 538 neither the mean R-values for scars and unfailed cliffs nor the mean R-values for fans
43 539 and unfailed cliffs differ significantly, suggesting that all the exposed surfaces are of
44 540 the same age (and relatively old). In the other three cases (fan Nos 46, 47 and 81) the
45 541 mean R-values of the scars and the fans are both significantly higher than the mean R-
46 542 values of the unfailed cliffs, confirming the SRSFs are younger than the exposure age
47 543 of the unfailed cliffs.
48 544

49 545 Comparison of the mean R-values from unfailed cliffs with the values from
50 546 the older control points given in Table 3 indicates that unfailed cliff surfaces were
51 547 exposed during or immediately after deglaciation at ~9700 cal. BP. As all surfaces
52 548 yielded mean R-values lower than those characteristic of the younger control points
53
54
55
56
57
58
59
60

(Table 4), it appears that fan deposition and scar exposure occurred throughout the Holocene and, in some cases, thousands of years after regional deglaciation. As a result, the temporal distribution of fan mean-R-values likely reflects the timing of single-event SRSF activity.

Temporal variations in SRSF activity

The age of each SRSF event, including its 95% confidence interval, is summarized graphically in Fig. 6A. Although there is some evidence of differences in the age distributions between the different valleys, there is no statistically significant correlation between SRSF age and altitude and no significant difference in age between aspects. The overall mean age of all 92 SRSF events is 5124 years, which equates with an average regional frequency of 1 in 105 years.

Simple age-frequency distributions of the SRSF events within the region as a whole are shown in Fig. 6B. Although these events occurred without any prolonged break in activity, their frequency varied considerably over the last ~10,000 years. The distribution based on 2000-yr time intervals has a single mode indicating an increase in the frequency of events through the early Holocene, a distinct peak in activity in the 6.0-4.0 ka time interval, and a consistent decline in activity thereafter. The use of 1000-year time intervals reveals two modes – at 8.0-7.0 and 5.0-4.0 ka, respectively. At least three modes can be recognized when 500-yr time intervals are used (at 9.0-8.5, 7.5-7.0 and 4.5-4.0 ka) and many more can possibly be discerned in the distribution based on 200-year time intervals. However, analysis of SRSF modes based on 200-year time intervals is not advisable, as this time interval (0.2 ka) is significantly smaller than the typical uncertainty of SRSF ages (~1 ka). Despite this, the hypothesis of an even distribution of SRSF events through time can be rejected at $p < 0.01$ irrespective of the age classes used.

The weighted age-frequency distribution (Fig. 6C) has four modes (at ~ 8.9, 7.3, 5.9 and 4.5 ka), which suggests that only four minor phases of enhanced SRSF frequency are meaningful. Furthermore, according to the weighted distribution, the frequency of events declines steadily after ~4.5 ka with no marked fluctuations.

The temporal pattern in the magnitude of the SRSFs (rock volume), as shown in in Fig. 6D, is substantially the same as the frequency distribution (compare with use of a 200-yr interval in Fig. 6B). In particular, the age-volume distribution has a similar major peak between 4.8 and 4.2 ka, and relatively little activity before 9.0 ka or after 1.0 ka.

Probability density function analysis indicates that the spread of SRSF ages does not conform to a normal distribution (Fig. 7A) and, instead, is best explained by 5 individual Gaussian age distributions (Fig. 7B). The sum of individual Gaussian distributions produces a re-integrated PDE which achieves a good model fit with the cumulative PDE. PDE analysis using < 5 individual Gaussian age distributions returns a poor ($n \leq 3$) or sub-optimal ($n = 4$) model fit. PDE analysis using > 5 individual Gaussian age distributions does not therefore significantly improve the model fit and instead risks over-interpretation of the number of SRSF modes. PDE analysis returns peak Gaussian ages (Fig. 7C) of 9.00 ± 1.13 ka ($n = 14$), 7.38 ± 0.99 ka ($n = 17$), 6.40 ± 0.77 ka ($n = 14$), 4.50 ± 1.42 ka ($n = 42$) and 1.90 ± 1.42 ka ($n = 18$). Although

1
2
3 599 these modes overlap with adjacent modes within 1σ , statistically significant
4 600 differences between sequential Gaussian age distributions are revealed by two-sample
5 601 Students t-tests ($p < 0.01$).
6 602

7 603 These Gaussian age distributions closely match the four modes identified in
8 604 weighted age-frequency analysis, with a dominant mode at ~ 4.5 ka (Fig. 7B). This
9 605 mode is the highest probability Gaussian distribution, comprises a significant number
10 606 of SRSF events ($n = 42$; Fig. 7D) and accounts for a large proportion of total SRSF
11 607 volume over the last ~ 10 ka ($18,744 \text{ m}^3$). In contrast to weighted age-frequency
12 608 analysis, PDE analysis returns an additional Gaussian age distribution during the late
13 609 Holocene at ~ 1.9 ka. However, this is unlikely to reflect a period of enhanced SRSF
14 610 activity as there is no clear clustering of SRSF ages (Fig. 7A), as evidenced by
15 611 weighted age-frequency analysis. Instead, late Holocene ages likely reflect declining
16 612 SRSF activity after the mid-Holocene peak.
17 613

18 614 The combined results of the age-frequency analyses and the Gaussian
19 615 separation achieved for PDEs demonstrate that SRSF occurrence through time is non-
20 616 uniform and multi-modal. Most notable is the high level of occurrence during the mid
21 617 Holocene, the clear statistical significance of which is confirmed by the results of
22 618 change detection analysis. The cumulative sum change detection graph (Fig. 8A)
23 619 shows a clear peak in the rate of SRSF intensity between 4.8 and 2.6 ka, significantly
24 620 exceeding the 2σ threshold, with the largest departure from background occurring at
25 621 4.3 ka. Conversely, SRSF intensity is significantly reduced beyond the negative 2σ
26 622 threshold during the late Holocene at 0.6–0.1 ka. These peaks are a significant
27 623 departure from the normal rate of occurrence during the Holocene. The three other
28 624 modes identified above as statistically significant must be regarded as relatively small
29 625 departures from background SRSF periodicity.
30 626

31 627 Meyer wavelet analysis was used to explore the two statistically significant
32 628 departures ($> 2\sigma$) from the background SRSF rate, as identified by change detection
33 629 analysis. The lowest frequency decomposed signal (d_6) is shown in Fig. 8C. The full
34 630 analysis record is provided in Supplementary Fig. 1.
35 631

36 632 Discussion

37 633 *Previous models of the timing of RSFs*

38 634
39 635
40 636
41 637 Widely different conceptual models can be proposed to describe and explain the
42 638 temporal distribution of Late Pleistocene and Holocene RSFs. A schematic
43 639 representation of several models, each of which links a distinctive pattern of change in
44 640 the frequency and/or magnitude of RSFs to one or more specific causes or triggers, is
45 641 shown in Fig. 9. Although they have been based mainly on MRSFs, these models are
46 642 introduced here as a basis for discussion of our Holocene SRSFs. It should be
47 643 emphasised, moreover, that RSFs may be multicausal and that most if not all of the
48 644 models have yet to be rigorously tested against data sets with a large number of
49 645 consistently dated RSFs.
50 646

51 647 *Model 1.* – The ‘continuity-of-activity model’ proposes that there are no significant
52 648 temporal variations in the frequency and/or magnitude of RSFs throughout the
53
54
55
56
57
58
59
60

1
2
3 649 Holocene. Despite the small number of dated RSFs available in most studies, few
4 650 authors have advocated this model. However, the model does appear to be consistent
5 651 with the temporal distribution of about 60 RSFs located in an extensive area of the
6 652 Alps centred on the Austrian Tyrol (Prager et al. 2008), which exhibits only limited
7 653 evidence of temporal clustering at ~10.5-9.4 ka and 4.2-3.0 ka. Prager et al. (2008)
8 654 attributed the continuity of activity to complex interactions between the processes
9 655 characterizing models 2-5 together with rock-strength degrading processes such as
10 656 time-dependent progressive fracture propagation that can both prepare and trigger
11 657 slope instabilities.
12 658

13
14 659 *Model 2.* – The ‘intermittent-earthquakes model’ is applicable to tectonically active
15 660 regions and assumes that RSFs are triggered directly by large-magnitude earthquakes
16 661 generated by tectonically-driven uplift or other crustal stresses. Such earthquakes are
17 662 essentially randomly distributed in time and therefore bear little or no relationship to
18 663 deglaciation, climate or any of the other potential causative factors in models 3-5 that
19 664 are effective in tectonically stable regions (see, for example, Fjeldskaar et al. 2000;
20 665 Hermanns et al. 2001; Keefer 2002, 2015; Hewitt et al. 2008; Antinao & Gosse 2009;
21 666 Stock & Uhrhammer 2010; Penna et al. 2011; McPhillips et al. 2014; Marc et al.
22 667 2015; Murphy 2015).
23 668

24 669 *Model 3.* – The ‘deglaciation-close-tracking model’ is characterised by a dominant
25 670 peak in RSF activity immediately (i.e. within the first millennium) following regional
26 671 deglaciation, with subsequent asymptotic decline in activity. The temporal pattern of
27 672 activity is therefore a typical paraglacial response (cf. Ballantyne 2002). Causal
28 673 factors that may account for such a pattern include glacial unloading, glacial
29 674 debuitressing, stress-release fracturing, enhanced groundwater pressure in rock joints
30 675 and permafrost degradation, all closely associated in time with deglaciation (Fischer
31 676 et al. 2006; Cossart et al. 2008; McColl 2012; McColl & Davies 2012; Ballantyne et
32 677 al. 2014a, 2014b; Böhme et al. 2015; Deline et al. 2015; Mercier et al. 2017).
33 678 Hermanns et al. (2017) found nearly half of 22 dated rock avalanches in southwest
34 679 Norway occurred within the first millennium following local deglaciation. Although
35 680 the majority of RSF events occur shortly after deglaciation, some occur much later,
36 681 due to time-dependent fracture propagation and progressive failure (e.g. Eberhardt et
37 682 al. 2004; Krautblatter et al. 2013; Phillips et al. 2017). The occurrence of recent RSFs
38 683 on glacier forelands following the retreat of mountain glaciers from their Little Ice
39 684 Age maximum limits provides some support for this model (Evans & Clague 1994;
40 685 Holm et al. 2004; Matthews & Shakesby 2004; Arsenault & Meigs 2005; Allen et al.
41 686 2010; Stoffel & Huggel 2012).
42 687

43 688 *Model 4.* – The ‘deglaciation-lagging model’ features a significantly delayed response
44 689 to deglaciation. Peak RSF activity typically occurs within a few millennia of
45 690 deglaciation and corresponds with maximum glacio-isostatic rebound (Hicks et al.
46 691 2000; Ballantyne & Stone 2013; Ballantyne et al. 2013, 2014a, 2014b; Cossart et al.
47 692 2014; Decaulne et al. 2016). The cause of RSF events is seen as fault reactivation and
48 693 fracture propagation triggered by earthquakes, the frequency of earthquakes and RSFs
49 694 generally diminishing through the Holocene as the rate of glacio-isostatic uplift
50 695 declines.
51 696

52 697 *Model 5.* – The ‘cool/wet-climate-response model’ applies particularly to the
53 698 Holocene, reflecting several possible effects of climatic variations on RSF activity.
54
55
56
57
58
59
60

699 Field monitoring, historical documentation and palaeo-studies indicate that
 700 precipitation variations can be a dominant trigger factor in the timing of RSFs but
 701 both cooler conditions and indirect effects such as variations in cleft water pressure,
 702 frost shattering and permafrost degradation have also been implicated in rock-slope
 703 instability (Eisbacher & Clague 1984; Matthews et al. 1997; Trauth et al. 2000, 2003;
 704 Dapples et al. 2003; Soldati et al. 2004; Prager et al. 2008; Crozier 2010; Borgatti &
 705 Soldati 2010; Blikra & Christiansen 2014; Zerathe et al. 2014; Johnson et al. 2017).
 706 Furthermore, Evans & Clague (1994), Huggel et al. (2010, 2012) and Stoffel &
 707 Huggel (2012) highlighted the possible effects of recent climate warming on RSFs,
 708 and direct solar heating of rock faces has also been examined as a possible trigger (cf.
 709 Allen & Huggel 2013; Collins & Stock 2016). In Fig. 7, model 5 assumes cool/wet
 710 conditions produce an increase in RSF activity, resulting in a strong rising trend
 711 through the late Holocene with fluctuations culminating in a Little Ice Age maximum
 712 of RSF activity.

713 714 *A new model of Holocene SRSF activity in Jotunheimen*

715
716 Based on analysis of Holocene SRSF activity in Jotunheimen and comparison with
 717 regional climatic and geo-environmental indicators, a new thermally-driven,
 718 permafrost-degradation model is proposed (Fig. 7, model 6). This model is
 719 characterized by several key elements:

- 720
- 721 • minimal activity following deglaciation in the early Holocene;
- 722 • maximum activity late in the mid Holocene on the multi-millennial timescale;
- 723 • declining activity through the late Holocene with a second minimum close to
724 the present;
- 725 • secondary fluctuations on multi-centennial to millennial timescales throughout
726 the Holocene;
- 727

728 This pattern of change bears little relationship to any of the previous models,
 729 which are clearly inappropriate in the context of these data. Model 1 can be rejected
 730 for Jotunheimen on the basis of the χ^2 tests in Table 5. Although there is an element of
 731 randomness in our data, and earthquakes do occasionally occur in this part of southern
 732 Norway, their magnitudes tend to be too low to be effective in triggering SRSFs
 733 inland from the seismically more active coastal and off-shore areas (cf. Bungum et al.
 734 2000; Fjeldskaar et al. 2000; Hicks et al. 2000; Olesen et al. 2000; Blikra et al. 2006).
 735 Moreover, there is no sign of a dominant early-Holocene activity peak in our
 736 histogram or change detection analysis, which is the characteristic feature of the two
 737 deglaciation-related models (3 and 4). Absence of an early peak may well be
 738 accounted for by considerable thinning of the Late Weichselian Ice Sheet prior to final
 739 deglaciation in Jotunheimen (Goehring et al. 2008; Mangerud et al. 2011; Hughes et
 740 al. 2016; Stroeven et al. 2016), which is likely to have reduced the scale of any
 741 paraglacial effects on RSFs after ~10.0 ka. For example, over half (56%) of the
 742 estimated glacio-isostatic rebound of 160 m that has taken place in Jotunheimen since
 743 12.0 ka was completed prior to 10.0 ka and a further quarter (26%) by 6.0 ka (Lyså
 744 et al. 2008). Finally, the temporal pattern of SRSF activity in Jotunheimen is negatively
 745 correlated with model 5, which indicates that cool/wet conditions should be rejected
 746 as the major cause of enhanced SRSF activity. Instead, this inverse pattern points to
 747 the counterintuitive conclusion that enhanced activity is linked to relatively warm
 748 climatic conditions.

749
750 *Association of SRSF activity with the thermal climate record*
751

752 The possible associations between enhanced Holocene SRSF activity and relatively
753 warm climatic conditions can be explored with reference to proxy temperature records
754 and reconstructions of temperature-sensitive geo-environmental indicators (Fig. 10A-
755 G).

756
757 The long-term annual air temperature trend for Northern Europe shown in Fig.
758 10B is a stacked pollen-based reconstruction expressed as deviations from the mean
759 (Seppä et al. 2009). The Holocene Thermal Maximum (HTM) is clearly expressed in
760 this figure from ~8.0 to 4.0 ka by mean annual temperatures consistently >0.5 °C
761 higher than today. Alkenone-based temperature reconstruction similarly documents
762 warmest sea-surface temperatures in the North Atlantic at this time (Eldevik et al.
763 2014; see also Jansen et al. 2008; Renssen et al. 2012). However, other
764 reconstructions based on chironomids (Velle et al. 2010), aquatic macrofossils
765 (Väliranta et al. 2015) and megafossils (Dahl & Nesje 1996; Paus & Haugland 2017),
766 which are not dependent on tree-pollen production or ocean temperatures, indicate
767 that the highest temperatures probably occurred at 10.0–8.0 ka. Mean summer
768 temperatures estimated from pine-tree limits in the Scandes Mountains (Dahl & Nesje
769 1996), for example, peak at ~1.5 °C above present temperatures around 9.0 ka (Fig.
770 10C). An early temperature maximum at ~9.0 ka is also shown in the pollen-based
771 reconstruction of July air temperature from Øvre Heimdalsvatnet in the low-alpine
772 belt of eastern Jotunheimen (Fig. 10D, Velle et al. 2010). At this location, a
773 temperature of at least 3.5 °C higher than present was attained by 9.0 ka, falling to the
774 long-term Holocene average by 4.0 ka. Comparison with these reconstructions
775 indicates that (1) SRSF frequency increased during the HTM and (2) maximum
776 activity was not reached until late in the HTM.

777
778 Three other palaeorecords can be used to focus on shorter-term warm intervals
779 comparable in scale with our minor phases of enhanced SRSF frequency (Fig. 10E-
780 G). The first of these (Fig. 10E), based on a standardized temperature reconstruction
781 derived from the record of $\delta^{18}\text{O}$ in the GISP 2 Greenland ice core (Alley 2004;
782 Wanner et al. 2011, their Fig. 1a), shows periods of above average air temperature.
783 Fig. 10F, based on the North Atlantic standardized stacked ocean ice-rafted debris
784 (IRD) record (Bond et al. 2001; Wanner et al. 2011, their Fig. 3a), shows periods
785 between IRD events, when sea-surface temperatures are likely to have been above the
786 long-term average. Both sets of warm periods demonstrate only moderate agreement
787 between themselves and with our minor phases of enhanced SRSF frequency. There is
788 poorer agreement (particularly in the late Holocene after ~3.0 ka) with the final
789 record, which relates to variations in the size of mountain glaciers in the study area
790 (Fig. 10G). Glacier variations are widely accepted as climate indicators that reflect, in
791 part, temporal variations in summer temperature, especially in the case of glaciers in
792 continental locations where winter precipitation variations tend to be less effective
793 than in maritime regions (Oerlemans 2005; Bakke et al. 2008; Nesje et al. 2008;
794 Winkler et al. 2010). Local glacier variations in the Smørstabbtindan massif,
795 Jotunheimen, which is centrally located in relation to the sites of our SRSF events in a
796 relatively continental region of southern Norway, exhibit at least nine Holocene time
797 intervals when the glaciers were smaller than they are today, including a prolonged
798 period from ~7.8 to 4.8 ka, which includes most of the HTM (Fig. 10G; Matthews &

799 Dresser 2008).

800
801 Thus, overall, a strong case can be made for linking millennial-scale variations
802 in SRSF activity to the thermal environment. However, causal mechanisms are
803 required to answer the following questions: (1) why was maximum SRSF activity
804 attained late in the mid-Holocene, rather than earlier in the HTM when temperatures
805 were at a maximum; and (2) why was there not a closer relationship between the
806 minor phases of enhanced SRSF activity and shorter-term warm periods, such as the
807 Mediaeval, Roman and Bronze Age warm periods, in particular during the late-
808 Holocene? We propose that permafrost degradation, and climate-dependent variation
809 in permafrost depth, can explain the temporal pattern of SRSF activity and, in
810 particular, the departure of the temporal pattern of SRSF activity from a simple
811 ‘warm-climate’ model.

812

813 *Conditionality of SRSF activity on permafrost degradation*

814

815 To interpret the results of both the change detection analysis and Meyer wavelet
816 analysis, a modelled permafrost record for Fennoscandia (Kukkonen & Šafanda 2001)
817 is used (Fig. 8B). This provides a basis for attributing SRSF activity in Jotunheimen
818 to permafrost degradation by focusing on relative changes to permafrost depth in
819 bedrock over the last ~10 ka. The 5% porosity model was selected for comparison as
820 this is more representative than the 0% porosity model given the numerous fractures
821 that lead to slope instability and SRSFs. The permafrost model shows a significant
822 decrease in depth beginning at ~8 ka and reaching a steady ‘shallow’ equilibrium by
823 ~5 ka. Permafrost is relatively stable from 5 ka until ~0.6 ka when permafrost depth
824 increases. This permafrost model is subdivided into five distinct periods and is related
825 to the SRSF record as follows:

826

827 *Phase 1: 10.0–8.1 ka (‘stable phase’).* – SRSF frequency is in equilibrium with
828 permafrost with no alarms detected in the change detection analysis and no low-order
829 oscillations in the Meyer wavelet record. Bedrock permafrost is stable throughout this
830 period and is used to define background Holocene depth. In this phase, persistent
831 bedrock permafrost acts to stabilize slopes and limit major SRSF activity.

832

833 *Phase 2: 8.1–4.8 ka (‘transition phase’).* – Progressive warming throughout the mid-
834 Holocene, as recorded in palaeo-climate reconstructions, acts to decrease permafrost
835 depth. In response, there is a minor progressive decrease in negative change detection
836 rates and increase in positive change detection within 2σ . This trend is matched by
837 Meyer wavelet analysis, with a progressive increase in SRSF frequency above the
838 Holocene background rate. In this phase, a gradual (~3 ka) but clear transition from
839 ‘deeper’ to ‘shallower’ permafrost (~28% depth change) is matched by a minor
840 increase in SRSF frequency and may explain the minor phases of enhanced SRSF
841 activity identified during this period. Moreover, this gradual change in permafrost
842 depth, as opposed to a stochastic response to climate warming, provides a compelling
843 explanation for the significant lag between SRSF activity and the HTM.

844

845 *Phase 3: 4.8–2.6 ka (‘peak phase’).* – Permafrost depth is more-or-less stable and
846 remains close to its minimum Holocene depth for ~2 ka. This period is matched by
847 SRSF activity, as change detection analysis records a significant, sustained and
848 positive rate of change ($> 2\sigma$) for ~2.2 ka, with a maximum attained at ~4.3 ka and

with SRSF frequency significantly exceeding the average frequency until ~ 3.3 ka ($> 6\sigma$). This change is matched by the Meyer wavelet record, with a peak at ~ 4.6 ka and a gradual decline to the Holocene background rate at ~ 2.5 ka. In this phase, persistent shallow permafrost may directly influence SRSF occurrence by (1) actively destabilizing bedrock cliffs and causing slope failure and/or (2) weakening bedrock cliffs and making them more susceptible to other trigger factors.

Phase 4: 2.6–0.6 ka ('exhaustion phase'). – Permafrost depth remains relatively stable and shallow for ~ 2 ka, with no significant deviation from modelled depths during the 'peak phase'. However, there is a clear decrease in SRSF frequency after the mid-Holocene peak with a return to the Holocene background rate, as revealed by both change detection and Meyer wavelet analysis. In this phase, we propose that bedrock cliffs have reached a new equilibrium with permafrost, as the majority of slopes that can fail under these permafrost conditions have failed by this time; that is, the supply of 'potentially failable' cliffs is exhausted. As a result, SRSF occurrence returns to an average frequency comparable with the 'stable phase' of the early Holocene.

Phase 5: 0.6 - 0.1 ka ('stabilization phase'). – Contrary to the dominant Holocene trend, this short-term late-Holocene phase shows a clear increase in permafrost depth after ~ 0.6 ka. This transition is coeval with a statistically significant decrease in SRSF frequency ($> 2\sigma$) while Meyer wavelet analysis records the continued decrease in frequency below the Holocene background level. These data suggest that an increase in bedrock permafrost depth directly controls SRSF activity by stabilizing slopes and decreasing the susceptibility of bedrock cliffs to direct or indirect failure.

The correlation between SRSF frequency and permafrost depth in bedrock as modeled by Kukkonen & Šafanda (2001) provides a compelling explanation for the low-frequency variations in SRSF activity during the Holocene and, in particular, for:

- the significant departure from mean Holocene SRSF frequency at the end of the mid Holocene;
- the lag between the HTM and the SRSF frequency peak;
- the low SRSF frequency in the early Holocene; and
- the marked decline in SRSF frequency near the end of the late Holocene (after ~ 0.6 ka).

These explanations are supported by change detection analysis and (d_6) Meyer wavelet analysis. A causal link between SRSF frequency and regional permafrost degradation is also supported by the close match between the altitudinal distribution of the 92 SRSFs and the current aspect-dependent lower altitudinal limit of permafrost in rock faces in the Galdhøpiggen massif (Hipp et al. 2014). Approximately 87% ($n = 80$) of SRSFs occur within ± 300 m of the limit and $\sim 62\%$ ($n = 57$) are ≤ 200 m below this limit. A small number of SRSFs are found above the permafrost limit ($\sim 16\%$; $n = 15$) but the majority are restricted to within ≤ 50 m above this limit. These data imply a causal relationship between SRSF occurrence and the time-dependent degradation and aggradation of bedrock permafrost during the Holocene, as driven by climate and locally controlled by aspect. Based on an altitudinal lapse rate of 0.6 °C per 100 m in mean annual air temperatures (MAAT), this implies that all SRSF sites would have been in the permafrost zone when temperatures were 3.0 °C lower than today. It is likely, therefore, that much of the permafrost that had survived or developed in SRSF

1
2
3 899 cliffs following deglaciation would have degraded during the HTM when MAAT is
4 900 likely to have reached 2.0–3.0 °C warmer than at present and when permafrost limits
5 901 would have been correspondingly higher (Lilleøren et al. 2012).
6 902

7 903 Higher-frequency changes in SRSF activity as reflected by weighted age-
8 904 frequency (Fig. 6C) and (d_1 - d_5) wavelet analysis (Supplementary Fig. 1) can be
9 905 interpreted as represent Holocene background SRSF frequency after removal of the
10 906 mid-Holocene positive peak and the late-Holocene negative peak of the change
11 907 detection analysis (Fig. 8A). These higher frequency changes are more challenging to
12 908 interpret, given the limited availability of palaeo-environmental records (e.g. seasonal
13 909 paleo-precipitation data, storm-event chronologies, palaeoseismic and groundwater
14 910 flux records) and the inherent SHD age uncertainties. The conceptual models related
15 911 to deglaciation and characterized by early-Holocene peak activity (Fig. 9) can be
16 912 discounted as these bear limited resemblance to the chronology of SRSF events.
17 913

18 914 Changes in permafrost depth might be expected to play a role in explaining the
19 915 higher-frequency changes. However, we cannot preclude a contribution to higher-
20 916 frequency variability from the continuity, earthquake, and cool/wet climate conceptual
21 917 models (Fig.9). Thawing permafrost may be a direct trigger factor for SRSF events
22 918 due, for example, to loss of strength or elevated hydrostatic pressure, or it may render
23 919 the rock slope susceptible to other triggers involving meltwater from spring snow melt
24 920 or extreme rainfall events in summer (Gruber et al. 2004; Gruber & Haerberli 2007;
25 921 Krautblatter et al. 2013; Blikra & Christiansen 2014; Draebing et al. 2014;
26 922 Krautblatter & Leith 2015; Messenzehl & Dikau 2017). Extreme summer rainfall
27 923 events, which are likely to have been more frequent during warm periods, have been
28 924 implicated in triggering debris-flow events in Leirdalen (Matthews et al. 2009) and
29 925 might have triggered some SRSFs.
30 926

31 927 *Further conceptual and methodological implications*

32 928

33 929 Thus, the timing of SRSFs in this study, with fluctuating SRSF activity rising to a
34 930 sustained peak at the transition from the mid- to late-Holocene, suggests the
35 931 importance of progressive but intermittent permafrost degradation lagging behind the
36 932 highest temperatures of the Holocene. Subsequent declining SRSF frequencies, in
37 933 contrast, appear to signal exhaustion of the supply of failable cliffs and/or renewed
38 934 aggradation of permafrost.
39 935

40 936 These fundamental findings recognize that Holocene SRSF activity in
41 937 Jotunheimen essentially reflects paraperiglacial processes: that is, it is a conditional
42 938 response to the transition from a permafrost to a seasonal-freezing climatic regime as
43 939 permafrost depth decreases (cf. Mercier 2008; Scarpozza 2016; Matthews et al. 2017).
44 940 While this model is primarily applicable to the SRSFs sampled in this study, it could
45 941 be tested in comparable mountain regions. In particular, links between permafrost
46 942 degradation and enhanced slope failure may explain SRSF frequency in regions with
47 943 comparable seismotectonics, glaciation and deglaciation histories or climatic trends.
48 944 Robust SRSF chronologies would need to be constructed to test the model, either
49 945 using radiometric methods (e.g. ^{10}Be) or calibrated-age dating techniques (e.g. SHD).
50 946

51 947 Our new SRSF chronology indicates, moreover, that SHD can be used to
52 948 generate reliable SRSF chronologies, although further work is necessary to verify this
53 949
54 950
55 951
56 952
57 953
58 954
59 955
60 956

1
2
3 949 technique by directly comparing age estimates for individual landforms derived from
4 950 both SHD and radiometric methods.

5 951
6 952 Finally, the recognition of a causal link between climate, permafrost
7 953 degradation and enhanced slope instability may have important implications for
8 954 glacial and periglacial environments under global warming scenarios. In particular,
9 955 while widespread retreat of mountain ice caps and valley glaciers may trigger initial
10 956 slope instability, our data suggest that the geomorphological impact of current
11 957 climatic and deglacial trends and, in particular, the slow transition from glacial to
12 958 periglacial, and to seasonal-freezing climatic regimes, may have a long-lasting impact
13 959 on mountain environments.

14 960

15 961

16 962 Conclusions

17 963

18 964 (1) We have developed an approach to the exposure-age dating of a large sample of
19 965 rock-slope failures, which involves adapting Schmidt-hammer exposure-age dating
20 966 (SHD) as a calibrated-age dating technique to the specific characteristics of small
21 967 rock-slope failures (SRSFs). SHD has provided an effective and low-cost method for
22 968 constructing a regional Holocene chronology of SRSFs (12 to 2520 m³) in the alpine
23 969 zone of Jotunheimen.

24 970

25 971 (2) Focusing on a large sample of SRSFs enables the detection of temporal variations
26 972 in the frequency and magnitude of events through the Holocene. Modes in a weighted
27 973 age-frequency distribution at ~8.9, 7.3, 5.9 and 4.5 ka were substantiated by
28 974 probability density function analysis, which produced individual Gaussian age
29 975 distributions of 9.00 ± 1.13 ka, 7.38 ± 0.99 ka, 6.40 ± 0.77 ka and 4.50 ± 1.42 ka.
30 976 Based on this analysis, SRSF activity was relatively low following deglaciation in the
31 977 early Holocene and attained a maximum towards the end of the mid Holocene (~4.5
32 978 ka). Peak SRSF activity lagged behind the Holocene Thermal Maximum by at least
33 979 ~2.2 ka and declined thereafter with a very low frequency of events during the last
34 980 millennium.

35 981

36 982 (3) Using change detection and discreet Meyer wavelet analysis in combination with
37 983 proxy temperature indicators and an existing permafrost depth model, we propose that
38 984 enhanced SRSF activity was primarily controlled by permafrost degradation. As a
39 985 result, the Holocene permafrost depth record is subdivided into five distinct periods
40 986 and related to the SRSF chronology as follows:

41 987

- 42 988 • 10 - 8.1 ka – ‘stable phase’ – low SRSF activity; maximum Holocene
43 989 permafrost depth.
- 44 990 • 8.1 - 4.8 ka – ‘transition phase’ – increasing susceptibility to SRSF activity;
45 991 decreasing permafrost depth.
- 46 992 • 4.8 - 2.6 ka – ‘peak phase’ – maximum SRSF activity; minimum Holocene
47 993 permafrost depth.
- 48 994 • 2.6 - 0.6 ka – ‘exhaustion phase’ – decreasing SRSF activity; little change in
49 995 shallow permafrost depth.
- 50 996 • 0.6 - 0.1 ka – ‘stabilization phase’ – minimum SRSF activity; increasing
51 997 permafrost depth.

52 998

53

54

55

56

57

58

59

60

1
2
3 999 (4) Long-term relative change in permafrost depth provides a compelling explanation
4 1000 for the high-magnitude departures from the SRSF background rate. In particular, the
5 1001 gradual change in permafrost depth during the ‘transition phase’, as opposed to a
6 1002 stochastic response to climate warming, accounts for the significant lag (~2.2 ka)
7 1003 between the Holocene Thermal Maximum and the SRSF frequency peak. Moreover,
8 1004 persistent shallow permafrost during the ‘peak phase’ may be the key driver behind
9 1005 SRSF occurrence by (a) actively destabilizing bedrock cliffs and causing slope failure
10 1006 and/or (b) weakening bedrock cliffs and making them more susceptible to other
11 1007 trigger factors.
12 1008

13 1009 (5) Conversely, declining SRSF frequency during the ‘exhaustion phase’ appears to
14 1010 reflect the diminished supply of potentially failable cliffs, even under a shallow
15 1011 permafrost depth scenario. Finally, low frequency of SRSF occurrence during the
16 1012 ‘stabilization phase’ likely reflects an increase in permafrost depth (permafrost
17 1013 aggradation) after ~0.6 ka; a change which would have been sufficient to stabilize
18 1014 slopes and decrease the susceptibility of bedrock cliffs to direct or indirect failure.
19 1015

20 1016 (6) This interpretation is supported by geomorphological evidence, given the
21 1017 consistent location of SRSF sites in relation to the local aspect-dependent lower
22 1018 altitudinal limit of permafrost in cliff faces. This new paraperiglacial model attributes
23 1019 enhanced SRSF activity to progressive and intermittent permafrost degradation during
24 1020 Holocene warm periods, including the possibility of renewed aggradation of
25 1021 permafrost during short-term cold periods and renewed degradation during the
26 1022 ensuing warm periods
27 1023

28 1024 (7) Our new thermally-driven, permafrost-degradation model of SRSF events in
29 1025 Jotunheimen bears little similarity to existing models of Holocene RSF activity.
30 1026 However, while aspects of this new model require further testing by other methods
31 1027 and in other regions, the results of this study have important implications for climate-
32 1028 change forcing of RSF activity. Projected mean annual global warming is predicted to
33 1029 decrease the area of mountain permafrost and raise lower altitudinal permafrost limits.
34 1030 This in turn will likely destabilize higher bedrock slopes and increase SRSF frequency
35 1031 there. The delayed response of peak SRSF frequency to warming climate, as
36 1032 modulated by permafrost depth, may therefore result in a long-lasting impact of
37 1033 current climate trends on mountain environments.
38 1034
39 1035

40 1036 *Acknowledgements* – Fieldwork was carried out on the Swansea University
41 1037 Jotunheimen Research Expeditions of 2014-2017. We are grateful to Ole and Tove
42 1038 Grindvold (Leirvassbu) for continuing expedition support; to Atle Nesje and Anne E.
43 1039 Bjune for data and sources of information on uplift rates and climate in southern
44 1040 Norway; and to R.L. Hermanns for a very thorough critical review that led to
45 1041 significant improvement of the manuscript. Anna C. Ratcliffe prepared the figures for
46 1042 publication. This paper constitutes Jotunheimen Research Expeditions, Contribution
47 1043 No. 205 (see <http://jotunheimenresearch.wixsite.com/home>).
48 1044
49 1045

50 1046 References

51 1047
52 1048 Aa, A.R. & Sjøstad, J.A. 2000: Schmidt hammer age evaluation of the moraine
53
54
55
56
57
58
59
60

- 1
2
3 1049 sequence in front of Bøyabreen, western Norway. *Norsk Geologiske Tidsskrift*
4 1050 80, 27-32.
- 5 1051 Aa, A.R., Sjøstad, J., Sønstegaard, E. & Blikra, L.H. 2007: Chronology of Holocene
6 1052 rock-avalanche deposits based on Schmidt-hammer relative dating and dust
7 1053 stratigraphy in nearby bog deposits, Vora, inner Nordfjord, Norway. *The*
8 1054 *Holocene* 17, 955-964.
- 9 1055 Ahlmann, H.W. 1922: Glaciers in Jotunheimen and their physiography. *Geografiska*
10 1056 *Annaler* 4, 1-57.
- 11 1057 Allen, S. & Huggel, C. 2013: Extremely warm temperatures as a potential cause of
12 1058 recent high mountain rockfall. *Global and Planetary Change* 107, 59-69.
- 13 1059 Allen, S., Cox, S. & Owens, I. 2010: Rock avalanches and other landslides in the
14 1060 central Southern Alps of New Zealand: a regional study considering possible
15 1061 climate change impacts. *Landslides* 8, 33-48.
- 16 1062 Alley, R.B. 2004: *GISP2 Ice Core Temperature and Accumulation Data*. IGBP
17 1063 *PAGES/World Data Center for Paleoclimatology Data Contribution Series*
18 1064 #2004-013. NOAA/NGDC Paleoclimate Program, Boulder, CO.
- 19 1065 André, M.F. 1996: Rock weathering rates in Arctic and subarctic environments
20 1066 (Abisko Mts, Swedish Lapland). *Zeitschrift für Geomorphology NF* 40, 499-
21 1067 517.
- 22 1068 André, M.F. 2002: Rates of postglacial rock weathering on glacially scoured outcrops
23 1069 (Abisko-Riksgränsen area, 68°N). *Geografiska Annaler Series A Physical*
24 1070 *Geography* 64, 139-150.
- 25 1071 Andreassen, L.M. & Winsvold, H., 2012. *Inventory of Norwegian Glaciers*.
26 1072 Norwegian Water Resources and Energy Directorate (NVE), Oslo.
- 27 1073 Antinao, J.L. & Gosse, J. 2009: Large rockslides in the southern central Andes of
28 1074 Chile (32–34°S): tectonic control and significance for Quaternary landscape
29 1075 evolution. *Geomorphology* 104, 117-133.
- 30 1076 Arsenault, A.M. & Meigs, A.J. 2005: Contribution of deep-seated bedrock landslides
31 1077 to erosion of a glaciated basin in southern Alaska. *Earth Surface Processes*
32 1078 *and Landforms* 30, 1111-1125.
- 33 1079 Aune, B. 1993: *Temperatur Normaler, Normalperiode 1961–1990*. Den Norske
34 1080 Meteorologiske Institutt, Oslo (Rapport 02/93, in Norwegian).
- 35 1081 Bakke, J., Lie, Ø., Dahl, S.O., Nesje, A. & Bjune, A.E. 2008: Strength and spatial
36 1082 patterns of the Holocene wintertime westerlies in the NE Atlantic region.
37 1083 *Global and Planetary Change* 60, 28-41.
- 38 1084 Ballantyne, C.K. 2002: Paraglacial geomorphology. *Quaternary Science Reviews* 21,
39 1085 1035-2017.
- 40 1086 Ballantyne, C.K. & Stone, J.O. 2013: Timing and periodicity of paraglacial rock-slope
41 1087 failures in the Scottish Highlands. *Geomorphology* 186, 150-161.
- 42 1088 Ballantyne, C.K., Wilson, P., Schnabel, C. & Xu, S. 2013: Lateglacial rock slope
43 1089 failures in north-west Ireland: age, causes and implications. *Journal of*
44 1090 *Quaternary Science* 28, 789-802.
- 45 1091 Ballantyne, C.K., Sandeman, G.F., Stone, J.O. & Wilson, P. 2014a: Rock-slope
46 1092 failure following Late Pleistocene deglaciation on tectonically stable
47 1093 mountainous terrain. *Quaternary Science Reviews* 86: 144-157.
- 48 1094 Ballantyne, C.K., Wilson, P., Gheorghiu, D. & Rodés, À. 2014b: Enhanced rock-slope
49 1095 failure following ice-sheet deglaciation: timing and causes. *Earth Surface*
50 1096 *Processes and Landforms* 39, 900-913.
- 51 1097 Barnett, C., Dumayne-Peaty, L. & Matthews, J.A. 2000: Holocene climatic change
52 1098 and tree-line response in Leirdalen, central Jotunheimen. *Review of*

- 1
2
3 1099 *Palaeobotany and Palynology* 117, 119-137.
- 4 1100 Barr, I.D., Roberson, S., Flood, R. & Dortch, J.M. 2017: Younger Dryas glaciers and
5 1101 climate in the Mourne Mountains, Northern Ireland. *Journal of Quaternary*
6 1102 *Science* 32, 104-115.
- 7 1103 Bates, R.L. & Jackson, J.A. (eds) 1987: *Glossary of Geology*, 3rd edition, 573.
8 1104 American Geological Institute: Alexandria, VA.
- 9 1105 Battey, M.H. & McRitchie, W.D. 1973: A geological traverse across the pyroxene-
10 1106 granulites of Jotunheimen in the Norwegian Caledonides. *Norsk Geologiske*
11 1107 *Tidsskrift* 53, 237-265.
- 12 1108 Battey, M.H. & McRitchie, W.D. 1975: The petrology of the pyroxene-granulite
13 1109 facies rocks of Jotunheimen. *Norsk Geologiske Tidsskrift* 55, 1-49.
- 14 1110 Benestad, R.E. 2005: Climate change scenarios for northern Europe from multi-modal
15 1111 IPCC AR4 climate simulations. *Geophysical Research Letters* 32, L17704.
- 16 1112 Betts, M.W. & Latta, M.A. 2000: Rock surface hardness as an indication of exposure
17 1113 age: an archaeological application of the Schmidt hammer. *Archaeometry* 42,
18 1114 209-223.
- 19 1115 Blikra, L.H. & Christiansen, H.H. 2014: A field-based model of permafrost-controlled
20 1116 rockslide deformation in northern Norway. *Geomorphology* 208, 34-49.
- 21 1117 Blikra, L.H., Longva, O., Braathen, A., Anda, E., Dehls, J.F. & Stalsberg, K. 2006:
22 1118 Rock slope failures in Norwegian fjord areas: examples, spatial distribution
23 1119 and temporal patterns. In Evans, S.G., Mugnozza, G.S., Strom, A. and
24 1120 Hermanns, R.L. (eds), *Landslides from Massive Rock Slope Failures*, 475-496.
25 1121 Springer: Dordrecht.
- 26 1122 Böhme, M., Oppikofer, T., Longva, O., Jaboyedorff, M., Hermanns, R.L. & Derron,
27 1123 M.-H. 2015. Analyses of past and present rock slope instabilities in a fjord
28 1124 valley: implications for hazard estimation. *Geomorphology* 248, 464-474.
- 29 1125 Bond, G., Kromer, B., Beer, J., Muscheler, R., Evans, M.N., Showers, W., Hoffmann,
30 1126 S., Lotti-Bond, R., Hajdas, R. & Bonani, G. 2001: Persistent solar influence on
31 1127 North Atlantic climate during the Holocene. *Science* 278, 1257-1266.
- 32 1128 Borgatti, L. & Soldati, M. 2010: Landslides and climatic change. In Alcántara-Ayala,
33 1129 I. & Goudie, A. (eds) *Geomorphological Hazards and Disaster Prevention*,
34 1130 87-95. Cambridge University Press, Cambridge.
- 35 1131 Braathen, A., Blikra, L.H., Berg, S.S. & Karlsen, F. 2004: Rock-slope failures in
36 1132 Norway: type, geometry, deformation mechanisms and stability. *Norwegian*
37 1133 *Journal of Geology* 84, 67-88.
- 38 1134 Brideau, M.-A. & Roberts, N.J. 2015: Mass movement in bedrock. In Davies, T. (ed.)
39 1135 *Landslide Hazards, Risks, and Disasters*, 43-90. Elsevier, Amsterdam.
- 40 1136 Briner, J.P., Kaufman, D.S., Manley, W.F., Finkel, R.C., & Caffee, M.W. 2005:
41 1137 Cosmogenic exposure dating of late Pleistocene moraine stabilization in
42 1138 Alaska. *Geological Society of America Bulletin* 117, 1108-1120.
- 43 1139 Brunnsden, D. & Prior, D.B. (eds) 1984: *Slope Instability*. Wiley, Chichester.
- 44 1140 Bungum, H., Lindholm, C.D., Dahle, A., Woo, G., Nadim, F., Holme, J.K.,
45 1141 Gudmestad, O.T., Hagberg, T. & Karthisgeyan, K. 2000: New seismic zoning
46 1142 maps for Norway, the North Sea, and the United Kingdom. *Seismological*
47 1143 *Research Letters* 71, 687-697.
- 48 1144 Černá, B. & Engel, Z. 2011: Surface and sub-surface Schmidt hammer rebound value
49 1145 variation for a granite outcrop. *Earth Surface Processes and Landforms* 36,
50 1146 170-170.
- 51 1147 Clague, J.J. & Stead, D. (eds) 2012: *Landslides: Types, Mechanisms and Modeling*,
52 1148 Cambridge University Press: Cambridge.

- 1
2
3 1149 Collins, B.D. & Stock, G.M. 2016: Rockfall triggering by cyclic thermal stressing of
4 1150 exfoliation fractures. *Nature Geoscience* 9, 395-399.
- 5 1151 Colman, S.M. 1981: Rock-weathering rates as functions of time. *Quaternary*
6 1152 *Research* 15, 250-264.
- 7 1153 Colman, S.M. & Dethier, D.P. (eds.) 1986: *Rates of Chemical Weathering of Rocks*
8 1154 *and Minerals*. Academic Press, Orlando, FL.
- 9 1155 Colman, S.M., Pierce, K.L. & Birkeland, P.W. 1987: Suggested terminology for
10 1156 Quaternary dating methods. *Quaternary Research* 28, 314-319.
- 11 1157 Cossart, E., Braucher, R., Fort, M., Bourlès, D.L. & Carcaillet, J. 2008: Slope
12 1158 instability in relation to glacial debuttressing in alpine areas (Upper Durance
13 1159 catchment, southeastern France): evidence from field data and ¹⁰Be cosmic
14 1160 ray exposure ages. *Geomorphology* 85, 3-26.
- 15 1161 Cossart, E., Mercier, D., Decaulne, A., Feuillet, T., Jónsson, H.P. & Þorsteinn
16 1162 Sæmundsson 2014: Impacts of post-glacial rebound on landslide spatial
17 1163 distribution at a regional scale in northern Iceland (Skagafjörður). *Earth*
18 1164 *Surface Processes and Landforms* 39, 336-353.
- 19 1165 Crosta, G.B. & Clague, J.J. 2009: Dating, triggering, modelling, and hazard
20 1166 assessment of large landslides. *Geomorphology* 103, 1-4. [Introduction to the
21 1167 Special Issue.]
- 22 1168 Crozier, M.J. 2010: Deciphering the effect of climate change on landslide activity: a
23 1169 review. *Geomorphology* 124, 260-267.
- 24 1170 Cruden, D.M. & Varnes, D.J. 2009: Landslide types and processes. In: Turner, A.K.
25 1171 & Schuster, R.L. (eds) *Landslides Investigation and Mitigation*.
26 1172 Transportation Research Board, US National Research Council: Washington,
27 1173 DC: Transportation Research Board, US National Research Council, pp. 36-
28 1174 75. [Special Report 247.]
- 29 1175 Dahl, S.O. & Nesje, A. 1996: A new approach to calculating Holocene winter
30 1176 precipitation by combining glacier equilibrium-line altitudes and pine-tree
31 1177 limits: A case study from Hardangerjøkulen, central-southern Norway. *The*
32 1178 *Holocene* 6, 381-398.
- 33 1179 Dahl, S.-O., Nesje, A., Lie, Ø., Fjordheim, K. & Matthews, J.A. 2002: Timing,
34 1180 equilibrium-line altitudes and climatic implications of two early-Holocene
35 1181 glacial re-advances during the Erdalen Event at Jostedalbreen, western
36 1182 Norway. *The Holocene* 12, 17-25.
- 37 1183 Dann, R., Close, M., Flintoft, M., Hector, R., Barlow, H., Thomas, S. & Francis, G.
38 1184 2009: Characterization and estimation of hydraulic properties in an alluvial
39 1185 gravel vadose zone. *Vadose Zone Journal* 8, 651-663.
- 40 1186 Dapples, F., Oswald, D., Raetzo, H., Landelli, T. & Zwahlen, P., 2003: New records of
41 1187 Holocene landslide activity in the Western and Eastern Swiss Alps:
42 1188 implications of climate and vegetation changes. *Eclogae Geologicae Helvetiae*
43 1189 96, 1-9.
- 44 1190 Davies, T. (ed.) 2015: *Landslide Hazards, Risks, and Disasters*. Elsevier, Amsterdam.
- 45 1191 Decaulne, A., Cossart, E., Mercier, D., Feuillet, T., Coquin, J. & Jónsson, H. 2016:
46 1192 An early Holocene age for the Vatn landslide (Skagafjörður, central northern
47 1193 Iceland): insights into the role of postglacial landsliding on slope development.
48 1194 *The Holocene* 26, 1304-1318.
- 49 1195 Deline, P. & Kirkbride, M.P. 2009: Rock avalanches on a glacier and morainic
50 1196 complex in Haut Val Ferret (Mont Blanc Massif, Italy). *Geomorphology* 103,
51 1197 80-92.

- 1
2
3 1198 Deline, P., Gruber, S., Delaloye, R., Fischer, L., Geertseema, M., Giardino, M.,
4 1199 Hasler, A., Kirkbride, M., Krautblatter, M., Magnin, F., NcColl, S., Raveland,
5 1200 L. & Schoeneich, P. 2015: Ice loss and slope stability in high-mountain
6 1201 regions. In Haeberli, W. & Whitman, C. (eds), *Snow and Ice-Related Hazards,*
7 1202 *Risks and Disasters*, 521-561. Elsevier, Amsterdam.
- 8 1203 Dera, Z.A. & Shumwayb, R.H. 1999: Phase onset time estimation at regional
9 1204 distances using the CUSUM algorithm. *Physics of the Earth and Planetary*
10 1205 *Interiors 113*, 227-246.
- 11 1206 Dortch, J.M., Owen, L.A., Haneberg, W.C., Caffee, M.W., Dietsch, C. & Kamp, U.
12 1207 2009: Nature and timing of large landslides in the Himalaya and
13 1208 Transhimalaya of northern India. *Quaternary Science Reviews 28*, 1037-1054.
- 14 1209 Dortch, J.M., Owen, L.A. & Caffee, M.W. 2013: Timing and climatic drivers for
15 1210 glaciation across semi-arid western Himalayan-Tibetan orogen. *Quaternary*
16 1211 *Science Reviews 78*, 188–208.
- 17 1212 Draebing, D., Krautblatter, M. & Dikau, R. 2014: Interaction of thermal and
18 1213 mechanical processes in steep permafrost rock walls: a conceptual approach,
19 1214 *Geomorphology 226*, 226-235.
- 20 1215 Eberhardt, E., Stead, D. & Coggan, J.S. 2004: Numerical analysis of initiation and
21 1216 progressive failure in natural rocks slopes: the 1991 Randa rockslide.
22 1217 *International Journal of Rock Mechanics and Mining Sciences 41*, 69-87.
- 23 1218 Eisbacher, G.H. & Clague, J.J. 1984: Destructive mass movements in high mountains:
24 1219 hazards and management. *Geological Survey of Canada, Paper 84/16*, 1-230.
- 25 1220 Eldevik, T., Risebrobakken, B., Bjune, A.E., Andersson, C., Birks, H.J.B., Dokken,
26 1221 T.M., Drange, H., Glessmer, M.S., Li, C., Nilsen, J.E.Ø., Ottera, O.H.,
27 1222 Richter, K. & Skagseth, Ø. 2014: A brief history of climate – the northern seas
28 1223 from the Last Glacial Maximum to global warming. *Quaternary Science*
29 1224 *Reviews 106*, 225-246.
- 30 1225 Etzelmüller, B., Berthling, I. & Sollid, J.L. 2003: Aspects and concepts on the
31 1226 geomorphological significance of Holocene permafrost in southern Norway.
32 1227 *Geomorphology 52*, 87-104.
- 33 1228 Evans, S.G. & Clague, J.J. 1994: Recent climate change and catastrophic geomorphic
34 1229 processes in mountain environments. *Geomorphology 10*, 107-128.
- 35 1230 Evans, S.G., Mugnozsa, G.S., Strom, A. & Hermanns, R.L. (eds) 2006: *Landslides*
36 1231 *from Massive Rock Slope Failures*. Springer, Dordrecht.
- 37 1232 Farbro, H., Hipp, T.F., Etzelmüller, B., Isaksen, K., Ødegård, R.S., Schuler, T.V. &
38 1233 Humlum, O. 2009: Air and ground temperature variations observed along
39 1234 elevation and continentality gradients in southern Norway. *Permafrost and*
40 1235 *Periglacial Processes 22*, 343–360.
- 41 1236 Fischer, L., Käab, A., Huggel, C. & Noetzli, J. 2006: Geology, glacier retreat and
42 1237 permafrost degradation as controlling factors of slope stability in a high
43 1238 mountain rock wall. *Natural Hazards and Earth System Sciences 6*, 761-772.
- 44 1239 Fjeldskaar, W., Lindholm, C., Dehls, J.F. & Fjeldskaar, I. 2000: Postglacial uplift,
45 1240 neotectonics and seismicity in Fennoscandia. *Quaternary Science Reviews 19*,
46 1241 1413-1422.
- 47 1242 Førland, E.J. 1993: *Nedbornormaler, Normalperiode 1961–1990*. Den Norske
48 1243 Meteorologiske Institutt, Oslo (Rapport 39//93, in Norwegian).
- 49 1244 Frattini, P., Crosta G.B. & Agliardi, F. 2012: Rockfall characterization and modeling.
50 1245 In Clague, J.J. & Stead, D. (eds), *Landslides: Types, Mechanisms and*
51 1246 *Modeling*, 267-271. Cambridge University Press: Cambridge.
- 52 1247 Gibbs, A.D. & Banham, P.H. 1979: *Sygnefjell Berggrunnsgeologisk kart 1518 III*,

- 1
2
3 1248 1:50,000. Norges Geologiske Undersøkelse, Trondheim.
- 4 1249 Ginås, K., Etzelmüller, B., Lussana, C., Hjort, J., Sannel, A.B.K., Isaksen, K.,
5 1250 Westermann, S., Kuhry, P., Christiansen, H., Frampton, A. & Åkerman, J.
6 1251 2017: Permafrost map for Norway, Sweden and Finland. *Permafrost and*
7 1252 *Periglacial Processes* 28, 359–378.
- 8 1253 Gjessing, J. 1967: Norway's paleic surface. *Norsk Geografisk Tidsskrift* 21, 69-132.
- 9 1254 Goehring, B.M., Brook, E.J., Linge, H., Raisbeck, G.M. & Yiou, F. 2008: Beryllium-
10 1255 10 exposure ages of erratic boulders in southern Norway and implications for
11 1256 the history of the Fennoscandian Ice Sheet. *Quaternary Science Reviews* 27,
12 1257 320-336.
- 13 1258 Goudarzi, M.A., Cocard, M., Santerre, R. & Woldai, T. 2013: GPS interactive time
14 1259 series analysis software. *GPS Solutions* 17, 595-603.
- 15 1260 Gruber, S. & Haeberli, W. 2007: Permafrost in steep bedrock slopes and its
16 1261 temperature-related destabilization following climate change. *Journal of*
17 1262 *Geophysical Research – Earth Surface* 112, F02S18. DOI:
18 1263 10.1029/2006JF000547.
- 19 1264 Gruber, S., Hoelzle, M. & Haeberli, W. 2004: Permafrost thaw and destabilization of
20 1265 Alpine rock walls in the hot summer of 2003. *Geophysical Research Letters*
21 1266 31, L13504. doi:10.1029/2004GL020051
- 22 1267 Hall, K., Thorn, C.E., Matsuoka, N. & Prick, A. 2002: Weathering in cold regions:
23 1268 some thoughts and perspectives. *Progress in Physical Geography* 26, 577-603.
- 24 1269 Hallet, B., & Putknonen, J. 1996: Surface dating of dynamic landforms: young
25 1270 boulders on aging moraines. *Science* 26, 937-940.
- 26 1271 Hallet, B., Walder, J.S. & Stubbs, C.W. 1991: Weathering by segregation ice growth
27 1272 in microcracks at sustained sub-zero temperatures: verification from an
28 1273 experimental study using acoustic emissions. *Permafrost and Periglacial*
29 1274 *Processes* 2, 283-300.
- 30 1275 Hermanns, R.L. & Longva, O. 2012: Rapid rock-slope failures. In Clague, J.J. &
31 1276 Stead, D. (eds): *Landslides: Types, Mechanisms and Modeling*, 59-70.
32 1277 Cambridge University Press: Cambridge.
- 33 1278 Hermanns, R.L., Trauth, M.H., Niedermann, S., McWilliams, M. & Strecker, M.R.
34 1279 2000: Tephrochronological constraints on temporal distribution of large
35 1280 landslides in Northwest Argentina. *Journal of Geology* 108, 35-52.
- 36 1281 Hermanns, R.L., Niedermann, S., Garcia, A.V., Gomez, J.S. & Strecker, M.R. 2001:
37 1282 Neotectonics and catastrophic failure of mountain fronts in the southern intra-
38 1283 Andean Puna Plateau, Argentina. *Geology* 29, 619-623.
- 39 1284 Hermanns, R.L., Niedermann, S., Ivy-Ochs, S. & Kubik, P.W. 2004: Rock
40 1285 avalanching into a landslide-dammed lake causing multiple dam failure in Las
41 1286 Conchas valley (NW Argentina) – evidence from surface exposure dating and
42 1287 stratigraphic analysis. *Landslides* 1, 113-122.
- 43 1288 Hermanns, R.L., Blikra, L.H., Naumann, M., Nilsen, B., Panthi, K.K. & Stromeyer,
44 1289 D. 2006: Examples from multiple rock-slope collapses from Köfels (Ötztal
45 1290 valley, Austria) and western Norway. *Engineering Geology* 83, 94-108.
- 46 1291 Hermanns, R.L., Schleier, M., Böhme, M., Blikra, L.H., Gosse, J., Ivy-Ochs, S. &
47 1292 Hilger, P. 2017: Rock-avalanche activity in W and S Norway peaks after the
48 1293 retreat of the Scandinavian Ice Sheet. In Mikoš, M., Vilímek, V., Yin, Y. &
49 1294 Sassa, K. (eds): *Advancing Culture of Living with Landslides, Volume 5:*
50 1295 *Landslides in Different Environments*, 331-338. Springer: Berlin.
- 51 1296 Hewitt, K., Clague, J.J. & Orwin, J.F. 2008: Legacies of catastrophic rock slope
52 1297 failures in mountain landscapes. *Earth-Science Reviews* 87, 1-38.

- 1
2
3 1298 Heyman, J., Stroeven, A.P., Harbor, J.M., & Caffee, M.W. 2011: Too young or too
4 1299 old: Evaluating cosmogenic exposure dating based on an analysis of compiled
5 1300 boulder exposure ages. *Earth and Planetary Science Letters* 302, 71-80.
6 1301 Hicks, E.C., Bungum, H. & Lindholm, C.D. 2000: Seismic activity, inferred crustal
7 1302 stresses and seismotectonics in the Rana region, Northern Norway.
8 1303 *Quaternary Science Reviews* 19, 1423-1436.
9 1304 Hipp, T., Etzelmüller, B. & Westermann, S. 2014: Permafrost in alpine rock faces
10 1305 from Jotunheimen and Hurrungane, southern Norway. *Permafrost and*
11 1306 *Periglacial Processes* 25, 1-13.
12 1307 Holm, K., Bovis, M. & Jakob, M. 2004: The landslide response of alpine basins to
13 1308 post-Little Ice Age glacial thinning and retreat in southwestern British
14 1309 Columbia. *Geomorphology* 57, 201-216.
15 1310 Hormes, A., Blaauw, Dahl, S.O., Nesje, A. & Possnert, G. 2009: Radiocarbon wiggle-
16 1311 match dating of proglacial lake sediments – implications for the 8.2 ka event.
17 1312 *Quaternary Geochronology* 4, 267-277.
18 1313 Huggel, C., Salzmann, N., Allen, S., Caplan-Auerbach, J., Fischer, L., Haeblerli, W.,
19 1314 Larsen, C., Schneider, D. & Wessel, R. 2010: Recent and future warm extreme
20 1315 events and high-mountain slope stability. *Philosophical Transactions of the*
21 1316 *Royal Society A* 368, 2435-2459.
22 1317 Huggel, C., Clague, J.J. & Korup, O. 2012: Is climate change responsible for
23 1318 changing landslide activity in high mountains? *Earth Surface Processes and*
24 1319 *Landforms* 37, 77-91.
25 1320 Hughes, A.L.C., Gyllencreutz, R., Lohne, Ø., Mangerud, J. & Svendsen, J.L. 2016:
26 1321 The last Eurasian ice sheets – a chronological database and time-slice
27 1322 reconstruction, DATED-1. *Boreas* 45, 1-45.
28 1323 Hungr, O. & Evans, S.G. 2004: Entrainment of debris in rock avalanches: analysis of
29 1324 a long run-out mechanism. *Geological Society of America Bulletin* 116, 1240-
30 1325 1252.
31 1326 Isaksen, K., Hauck, C., Gudevang, E., Ødegård, R.S. & Sollid, J.L. 2002: Mountain
32 1327 permafrost distribution in Dovrefjell and Jotunheimen, southern Norway,
33 1328 based on BTS and DC resistivity tomography data. *Norsk Geografisk Tidsskrift*
34 1329 *56*, 122-136.
35 1330 Ivy-Ochs, S., Poschinger, A.v., Synal, H. & Maisch, M. 2009: Surface exposure
36 1331 dating of the Flims landslide, Graubünden, Switzerland. *Geomorphology* 103,
37 1332 104-112.
38 1333 Jansen, E., Andersson, C., Moros, M., Nisancioglu, K.H., Nyland, B.F. & Telford,
39 1334 R.J. 2008: The early to mid-Holocene thermal optimum in the North Atlantic.
40 1335 In Battarbee, R.W. & Binney, H.A. (eds): *Natural Climate Variability and*
41 1336 *Global Warming: a Holocene Perspective*, 128-137. Wiley-Blackwell:
42 1337 Chichester.
43 1338 Jarman, D. 2006: Large rock slope failures in the Highlands of Scotland:
44 1339 characterization, causes and spatial distribution. *Engineering Geology* 83, 161-
45 1340 182.
46 1341 Johnson, B.G., Smith, J.A. & Diemer, J.A. 2017: A chronology of post-glacial
47 1342 landslides suggests that slight increases in precipitation could trigger a
48 1343 disproportionate geomorphic response. *Earth Surface Processes and*
49 1344 *Landforms* 42, 2223-2239.
50 1345 Karlén, W. & Matthews, J.A. 1992: Reconstructing Holocene glacier variations from
51 1346 glacial lake sediments: studies from Nordvestlandet and Jostedalbreen-

- 1
2
3 1347 Jotunheimen, southern Norway. *Geografiska Annaler Series A Physical*
4 1348 *Geography* 74, 327-348.
- 5 1349 Keefer, D.K. 2002: Investigating landslides caused by earthquakes – a historical
6 1350 review. *Surveys in Geophysics* 23, 473-510.
- 7 1351 Keefer, D.K. 2015: Landslides generated by earthquakes: immediate and long-term
8 1352 effects. In Owen, L.A. (ed.) *Tectonic Geomorphology*, 250-266. Elsevier,
9 1353 Amsterdam. [Treatise on Geomorphology, Volume 5]
- 10 1354 Korup, O., Clague, J.J., Hermanns, R.L., Hewitt, K., Strom, A.L., & Weidinger, J.T.
11 1355 2007: Giant landslides, topography, and erosion. *Earth and Planetary Science*
12 1356 *Letters* 261, 578-589
- 13 1357 Krautblatter, M. & Leith, K. 2015: Glacier- and permafrost-related slope instabilities.
14 1358 In Huggel, C., Carey, M., Clague, J.J. & Kääh, A. (eds): *The High-Mountain*
15 1359 *Cryosphere: Environmental Changes and Human Risks*, 147-165. Cambridge
16 1360 University Press, Cambridge.
- 17 1361 Krautblatter, M., Funk, D. & Guenzel, F. 2013: Why permafrost rocks become
18 1362 unstable: a rock-ice-mechanical model in time and space. *Earth Surface*
19 1363 *Processes and Landforms* 38, 876-887.
- 20 1364 Kukkonen, I.T., & Šafanda, J. 2001: Numerical modelling of permafrost in bedrock in
21 1365 northern Fennoscandia during the Holocene. *Global and Planetary Change* 29,
22 1366 259-273.
- 23 1367 Lang, A., Moya, J. Corominas, J., Schrott, L. & Dikau, R. 1999: Classic and new
24 1368 dating methods for assessing the temporal occurrence of mass movements.
25 1369 *Geomorphology* 30, 33-52.
- 26 1370 Lau, K.-M., & Weng, H. 1995: Climate signal detection using wavelet transform:
27 1371 How to make a time series sing. *Bulletin of the American Meteorological*
28 1372 *Society* 76, 2391-2402.
- 29 1373 Lidmar-Bergström, K., Ollier, C. & Sulebak, J.R. 2000: Landforms and uplift history
30 1374 of southern Norway. *Global and Planetary Change* 24, 211-231.
- 31 1375 Lilleøren, K.S., Etzelmüller, B., Schuler, T.V., Ginås, K. & Humlum, O. 2012: The
32 1376 relative age of permafrost – estimation of Holocene permafrost limits in
33 1377 Norway. *Global and Planetary Change* 92–93, 209–223.
- 34 1378 Lu, M., Pebesma, E., Sanchez, A. & Verbesselt, J. 2016: Spatio-temporal change
35 1379 detection from multidimensional arrays: Detecting deforestation from MODIS
36 1380 time series. *ISPRS Journal of Photogrammetry and Remote Sensing* 117, 227-
37 1381 236.
- 38 1382 Luckman, B.L. 2004: Rockfall. In Goudie, A.S. (ed.): *Encyclopedia of*
39 1383 *Geomorphology, Volume 2*, 882. Routledge: London.
- 40 1384 Lutro, O. & Tveten, E. 1996: *Geologiske kart over Norge, bergrunnskart Årdal*,
41 1385 1:250,000. Norges Geologiske Undersøkelse, Trondheim.
- 42 1386 Lyså A., Knies, J. & Larsen E. 2008: Kunnskap om istider og landformer – nøkkelen til
43 1387 forståelsen av klimavariasjoner. *Gråsteinen* 12, 41-57. [Norges geologiske
44 1388 undersøkelse]
- 45 1389 Mangerud, J., Gyllencreutz, R., Lohne, Ø. & Svendsen, J.I. 2011: Glacial history of
46 1390 Norway. In Ehlers, J., Gibbard, P.L. & Hughes, P.D. (eds): *Quaternary*
47 1391 *glaciations – extent and chronology: a closer look*, 279-298. Elsevier:
48 1392 Amsterdam.
- 49 1393 Marc, O., Hovius, N., Meunier, P., Uchida, T. & Hayashi, S. 2015: Transient changes
50 1394 of landslide rates after earthquakes. *Geology* 43, 883-886.
- 51 1395 MATLAB 2015. *MATLAB Version 8.5*, The MathWorks, Inc., Natick MA.
- 52 1396 Matsuoka, N. & Murton, J. 2008: Frost weathering: recent advances and future

- 1
2
3 1397 directions. *Permafrost and Periglacial Processes* 19, 195-210.
- 4 1398 Matthews, J.A. 1991: The late Neoglacial ('Little Ice Age') glacier maximum in
5 1399 southern Norway: new ¹⁴C-dating evidence and climatic implications. *The*
6 1400 *Holocene* 1, 219-133.
- 7
8 1401 Matthews, J.A. 2005: 'Little Ice Age' glacier variations in Jotunheimen, southern
9 1402 Norway: a study in regionally-controlled lichenometric dating of recessional
10 1403 moraines with implications for climate and lichen growth rates. *The*
11 1404 *Holocene* 15, 1-19.
- 12
13 1405 Matthews, J.A. & Dresser, P.Q. 2008: Holocene glacier variation chronology of the
14 1406 Smørstabbtindan massif, Jotunheimen, southern Norway, and the recognition
15 1407 of century- to millennial-scale European Neoglacial events. *The Holocene* 18,
16 1408 181-201.
- 17 1409 Matthews, J.A. & McEwen, L.J. 2013: High-precision Schmidt-hammer exposure-age
18 1410 dating (SHD) of flood berms, Vetlestølsdalen, alpine southern Norway: first
19 1411 application and some methodological issues. *Geografiska Annaler Series A*
20 1412 *Physical Geography* 95, 185-194.
- 21 1413 Matthews, J.A. & Owen, G. 2008: Endolithic lichens, rapid biological weathering and
22 1414 Schmidt hammer R-values on recently exposed rock surfaces: Storbreen
23 1415 glacier foreland, Jotunheimen, Norway. *Geografiska Annaler Series A*
24 1416 *Physical Geography* 90, 287-297.
- 25 1417 Matthews, J.A. & Owen, G. 2010: Schmidt-hammer exposure-age dating: developing
26 1418 linear age-calibration curves using Holocene bedrock surfaces from the
27 1419 Jotunheimen–Jostedalbreen regions of southern Norway. *Boreas* 39, 105-115.
- 28 1420 Matthews, J.A. & Owen, G. 2011: Holocene chemical weathering, surface lowering
29 1421 and rock weakening rates on glacially eroded bedrock surfaces in an alpine
30 1422 periglacial environment, Jotunheimen, Norway. *Permafrost and Periglacial*
31 1423 *Processes* 22, 279-290.
- 32
33 1424 Matthews, J.A. & Seppälä, M. 2005: Holocene colluvial chronology in the sub-arctic
34 1425 esker landscape at Kuttanen, Finnisj Lapland: kettleholes as geo-ecological
35 1426 archives of interactions amongst fire, vegetation, soil, climate and
36 1427 geomorphological instability. *Boreas* 44, 343-367.
- 37 1428 Matthews, J.A. & Shakesby, R.A., 1984: The status of the 'Little Ice Age' in southern
38 1429 Norway: relative-age dating of Neoglacial moraines with Schmidt hammer and
39 1430 lichenometry. *Boreas* 13, 333-346.
- 40 1431 Matthews, J.A. & Shakesby, R.A. 2004: A twentieth-century neoparaglacial rock topple
41 1432 on a glacier foreland, Ötztal Alps, Austria. *The Holocene* 14, 454-458.
- 42 1433 Matthews, J.A. & Vater, A.E. 2015: Pioneer zone geo-ecological change:
43 1434 observations from a chronosequence on the Storbreen glacier foreland,
44 1435 Jotunheimen, southern Norway. *Catena* 135, 219-230.
- 45 1436 Matthews, J.A. & Wilson, P. 2015: Improved Schmidt-hammer exposure ages for
46 1437 active and relict pronival ramparts in southern Norway, and their
47 1438 palaeoenvironmental implications. *Geomorphology* 246, 7-21.
- 48 1439 Matthews, J.A. & Winkler, S. 2011: Schmidt-hammer exposure-age dating (SHD):
49 1440 application to early Holocene moraines and a reappraisal of the reliability of
50 1441 terrestrial cosmogenic-nuclide dating (TCND) at Austanbotnbreen,
51 1442 Jotunheimen, Norway. *Boreas* 40, 256-270.
- 52
53 1443 Matthews, J.A., Brunsden, D., Frenzel, B., Gläser, B. & Weiss, M.M. (eds) 1997: *Rapid*
54 1444 *Mass Movement as a Source of Climatic Evidence for the Holocene*. Gustav
55 1445 Fisher Verlag, Stuttgart, 446 pp. [*Paläoklimaforschung* Volume 19]

- 1
2
3 1446 Matthews J.A., Berrisford, M.S., Dresser, P.Q., Nesje, A., Dahl, S.O., Bjune, A.E.,
4 1447 Bakke, J., Birks, H.J.B., Lie, Ø., Dumayne-Peaty, L. & Barnett, C. 2005:
5 1448 Holocene glacier history of Bjørnbreen and climatic reconstruction in central
6 1449 Jotunheimen, southern Norway, based on proximal glaciofluvial stream-bank
7 1450 mires. *Quaternary Science Reviews* 24, 67-90.
- 8 1451 Matthews, J.A., Dahl, S.O., Dresser, P.Q., Berrisford, M.S., Lie, Ø., Nesje, A. &
9 1452 Owen, G. 2009: Radiocarbon chronology of Holocene colluvial (debris-flow)
10 1453 activity at Sletthamn, Jotunheimen, southern Norway: a window on the
11 1454 changing frequency of extreme climatic events and their landscape impact.
12 1455 *The Holocene* 19, 1107-1129.
- 13 1456 Matthews, J.A., Nesje, A. & Linge, H. 2013: Relict talus-foot rock glaciers at
14 1457 Øyberget, upper Ottadalen, southern Norway: Schmidt hammer exposure ages
15 1458 and palaeoenvironmental implications. *Permafrost and Periglacial Processes*
16 1459 24, 336-346.
- 17 1460 Matthews, J.A., Winkler, S. & Wilson, P. 2014: Age and origin of ice-cored moraines
18 1461 in Jotunheimen and Breheimen, southern Norway: insights from Schmidt-
19 1462 hammer exposure-age dating. *Geografiska Annaler Series A Physical*
20 1463 *Geography* 96, 531-548.
- 21 1464 Matthews, J.A., McEwen, L.J. & Owen, G. 2015: Schmidt-hammer exposure-age
22 1465 dating (SHD) of snow-avalanche impact ramparts in southern Norway:
23 1466 approaches, results and implications for landform age, dynamics and
24 1467 development. *Earth Surface Processes and Landforms* 40, 1705–1718.
- 25 1468 Matthews, J.A., Owen, G., Winkler, S., Vater, A.E., Wilson, P., Mourne, R.W. & Hill,
26 1469 J.L. 2016: A rock-surface microweathering index from Schmidt hammer R-
27 1470 values and its preliminary application to some common rock types in southern
28 1471 Norway. *Catena* 143, 35-44.
- 29 1472 Matthews, J.A., Wilson, P. & Mourne, R.W. 2017: Landform transitions from
30 1473 pronival ramparts to moraines and rock glaciers: a case study from the
31 1474 Smørbotn cirque, Romsdalsalpane, southern Norway. *Geografiska Annaler*
32 1475 *Series A Physical Geography* 96, 15-37.
- 33 1476 McCarroll, D. 1987: The Schmidt hammer in geomorphology: five sources of
34 1477 instrument error. *British Geomorphological Research Group Technical*
35 1478 *Bulletin* 36, 16-27.
- 36 1479 McCarroll, D. 1994: The Schmidt hammer as a measure of degree of rock surface
37 1480 weathering and terrain age. In Beck, C. (ed.) *Dating in Exposed and Surface*
38 1481 *Contexts*, 29-45. University of New Mexico Press, Albuquerque.
- 39 1482 McColl, S.T. 2012: Paraglacial rock-slope stability. *Geomorphology* 153-154, 1-16.
- 40 1483 McColl, S.T. & Davies T.R.H. 2012: Large ice-contact slope movements, glacial
41 1484 buttressing, deformation and erosion. *Earth Surface Processes and Landforms*
42 1485 38, 1102-1115.
- 43 1486 McPhillips, D., Bierman, P.R. & Rood, D.H. 2014: Millennial-scale record of
44 1487 landslides in the Andes consistent with earthquake trigger. *Nature Geoscience*
45 1488 7, 925-930.
- 46 1489 Mercier, D. 2008: Paraglacial and paraperiglacial land systems: concepts, temporal
47 1490 scales and spatial distribution. *Géomorphologie: Relief, Processus,*
48 1491 *Environnement* 14, 223-233.
- 49 1492 Mercier, D., Coquin, J., Feuillet, T., Decaulne, A., Cossart, E., PallJónsson, H. &
50 1493 Sæmundsson, Þ. 2017: Are Icelandic rock-slope failures paraglacial? Age
51 1494 evaluation of seventeen rock-slope failures in the Skagafjörður area based on
52 1495 geomorphological stacking, radiocarbon dating and tephrochronology.

- 1
2
3 1496 *Geomorphology* 296, 45-58.
- 4 1497 Messenzehl, K. & Dikau, R. 2017: Structural and thermal controls of rockfall
5 1498 frequency and magnitude within rockwall-talus systems (Swiss Alps). *Earth*
6 1499 *Surface Processes and Landforms* 42, 1963-1981.
- 7 1500 Moen, A. 1999: *National Atlas of Norway: Vegetation*. Norwegian Mapping
8 1501 Authority, Hønefoss.
- 9 1502 Moreiras, S.M., Hermanns, R.L. & Fauqué, L. 2015: Cosmogenic dating of rock
10 1503 avalanches constraining Quaternary stratigraphy and regional neotectonics in
11 1504 the Argentine Central Andes (32°S). *Quaternary Science Reviews* 112, 45-58.
- 12 1505 Moses, C., Robinson, D. & Barlow, J. 2014: Methods for measuring rock surface
13 1506 weathering and erosion: a critical review. *Earth-Science Reviews* 135, 141-
14 1507 161.
- 15 1508 Murari, M.K., Owen, L.A., Dortch, J.M., Caffee, M.W., Dietsch, C., Fuchs, M.,
16 1509 Haneberg, W.C., Sharma, M.C. & Townsend-Small, A. 2014: Timing and
17 1510 climatic drivers for glaciation across monsoon-influenced regions of the
18 1511 Himalayan-Tibetan orogen. *Quaternary Science Reviews* 88, 159-182.
- 19 1512 Murphy, B. 2015: Coseismic landslides. In Davies, T. (ed.) *Landslide Hazards, Risks,*
20 1513 *and Disasters*, 91-129. Elsevier, Amsterdam.
- 21 1514 Murton, J. B., Peterson & Ozouf, J.-C. 2006: Bedrock fracture in cold regions.
22 1515 *Science* 314, 1127-1129.
- 23 1516 Nesje, A. 2009: Late Pleistocene and Holocene alpine glacier fluctuations in
24 1517 Scandinavia. *Quaternary Science Reviews* 28, 2119-2136.
- 25 1518 Nesje, A. & Dahl, S.O. 2001: The Greenland 8200 cal. yr BP event detected in loss-
26 1519 on-ignition profiles in Norwegian lacustrine sediment sequences. *Journal of*
27 1520 *Quaternary Science* 16, 155-166.
- 28 1521 Nesje, A., Bakke, J., Dahl, S.O., Lie, Ø. & Matthews, J.A. 2008: Norwegian glaciers
29 1522 in the past, present and future. *Global and Planetary Change* 60, 10-27.
- 30 1523 Nesje, A., Blikra, L. & Anda, E. 1994: Dating rockfall-avalanche deposits from
31 1524 degree of rock-surface weathering by Schmidt-hammer tests: a study from
32 1525 Norangsdalen, Sunnmøre, Norway. *Norsk Geologiske Tidsskrift* 74, 108-113.
- 33 1526 Nicholson, D.T. 2008: Rock control in microweathering of bedrock surfaces in a
34 1527 periglacial environment. *Geomorphology* 101, 655-665.
- 35 1528 Nicholson, D.T. 2009: Holocene microweathering rates and processes on ice-eroded
36 1529 bedrock, Røldal area, Hardangervidda, southern Norway. In: Knight, J. &
37 1530 Harrison, S. (eds.): *Periglacial and Paraglacial Processes and Environments*,
38 1531 29-49. Geological Society, Special Publication 320. Geological Society of
39 1532 London, Bath.
- 40 1533 Ødgård, R.S., Sollid, J.L. & Liestøl, O. 1992: Ground temperature measurements in
41 1534 mountain permafrost, Jotunheimen, southern Norway. *Permafrost and*
42 1535 *Periglacial Processes* 3, 231-234.
- 43 1536 Ødgård, R.S., Nesje, A., Isaksen, K., Andreassen, L.M., Eiken, T., Scwikowski, M. &
44 1537 Uglietti, C. 2017: Climate change threatens archaeologically significant ice
45 1538 patches: insights into their age, internal structure, mass balance and climate
46 1539 sensitivity. *The Cryosphere* 11, 17-32.
- 47 1540 Oerlemans, J. 2005: Extracting a climate signal from 169 glacier records. *Science* 308,
48 1541 675-677.
- 49 1542 Olesen, O., Dehls, J., Bugum, H., Riis, F., Hicks, E., Lindholm, C., Blikra, L.H.,
50 1543 Fjeldskaar, W., Olsen, L., Longva, O., Faleide, J.I., Bockmann, L., Rise, L.,
51 1544 Roberts, D., Braathen, A. & Brekke, H. 2000: *NEONOR: Neotectonics in*
52 1545 *Norway, Final Report*. Norges Geologiske Undersøkelse, Trondheim. [Report

- 1
2
3 1546 2000.002]
- 4 1547 Owen, G., Hiemstra, J.F., Matthews, J.A. and McEwen, L.J. 2010: Landslide-glacier
5 1548 interaction in a neoparaglacial setting at Tverrbytnede, Jotunheimen, southern
6 1549 Norway. *Geografiska Annaler Series A Physical Geography* 92, 421-436.
- 7 1550 Pánek, T. 2014: Recent progress in landslide dating: a global overview. *Progress in*
8 1551 *Physical Geography* 39, 168-198.
- 9 1552 Paus, A. & Haugland, V. 2017: Early- to mid-Holocene forest-line and climate
10 1553 dynamics in southern Scandes mountains inferred from contrasting megafossil
11 1554 and pollen data. *The Holocene* 27, 361-383.
- 12 1555 Penna, I.M., Hermanns, R.L., Niedermann, S & Folguera, A. 2011: Multiple slope
13 1556 failures associated with neotectonic activity in the Southern Central Andes
14 1557 (37°-37° 30'S), Patagonia, Argentina. *Geological Society of America Bulletin*
15 1558 123, 1880-1895.
- 16 1559 Phillips, M., Wolter, A., Lüthi, R., Amann, F., Kenner, R. & Bühler, Y. 2017: Rock
17 1560 slope failure in a recently deglaciated permafrost rock wall at Piz Kesch
18 1561 (Eastern Swiss Alps), February 2014. *Earth Surface Processes and Landforms*
19 1562 42, 426-438.
- 20 1563 Prager, C., Zangerl, C., Patzelt, G. & Brandner, R. 2008: Age distribution of fossil
21 1564 landslides in the Tyrol (Austria) and its surrounding areas. *Natural Hazards*
22 1565 *and Earth System Sciences* 8, 377-407.
- 23 1566 Prager, C., Ivy-Ochs, S., Ostermann, M., Synal, H.-A. & Patzelt, G. 2009: Geology
24 1567 and radiometric ¹⁴C-, ³⁶Cl- and Th/U-dating of the Fernpass rockslide (Tyrol,
25 1568 Austria). *Geomorphology* 103, 93-103.
- 26 1569 Proceq 2004: *Operating instructions. Betonprüfhammer N/NR-L/LR*. Proceq SA:
27 1570 Schwerzenbach.
- 28 1571 Rapp, A. 1960a: Talus slopes and mountain walls at Templefjorden, Spitzbergen.
29 1572 *Norsk Polarinstitutt Skrifter* 119, 1-96.
- 30 1573 Rapp, A. 1960b: Recent development of mountain slopes in Kärkevagge and
31 1574 surroundings, northern Scandinavia. *Geografiska Annaler* 42, 65-200.
- 32 1575 Reimer, P.J., Bard, E., Bayliss, A., Beck, J.W., Blackwell, P.G., Ramsey, C.B., Buck,
33 1576 C.E., Cheng, H., Edwards, R.L., Friedrich, M. & Grootes, P.M. 2013: IntCal13
34 1577 and Marine13 radiocarbon age calibration curves 0–50,000 years cal BP.
35 1578 *Radiocarbon* 55, 1869-1887.
- 36 1579 Renssen, H., Seppä, H., Crosta, X., Goose, H. & Roche, D.M. 2012: Global
37 1580 characterization of the Holocene Thermal Maximum. *Quaternary Science*
38 1581 *Reviews* 48, 7-19.
- 39 1582 Sánchez, S.J., Mosquera, D.F & Vidal Romani, J.R. 2009: Assessing the age-
40 1583 weathering correspondence of cosmogenic ²¹Ne dated Pleistocene surfaces by
41 1584 the Schmidt hammer. *Earth Surface Processes and Landforms* 34, 1121-1125.
- 42 1585 Sandøy, G., Oppikofer, T. & Nilsen, B. 2017: Why did the 1756 Tjellefonna rockslide
43 1586 occur? A back-analysis of the largest historic rockslide in Norway.
44 1587 *Geomorphology* 289, 78-95.
- 45 1588 Sass, O. & Wollny, K. 2001: Investigations regarding alpine talus slopes using
46 1589 ground-penetrating radar (GPR) in the Bavarian Alps, Germany. *Earth Surface*
47 1590 *Processes and Landforms* 26, 1071-1086.
- 48 1591 Scarpozza, C. 2016: Evidence of paraglacial and paraperiglacial crisis in Alpine
49 1592 sediment transfer since the last glaciation (Tincino, Switzerland). *Quaternaire*
50 1593 27, 139-155.
- 51 1594 Schleier, M., Hermanns, R.L., Rohn, J. & Gosse J.C. 2015: Diagnostic characteristics
52 1595 and paleodynamics of supraglacial rock avalanches, Innerdalen, Western

- 1
2
3 1596 Norway. *Geomorphology* 245, 23-39.
- 4 1597 Schleier, M., Hermanns, R.L., Goose, J.C., Oppikofer, T., Rohn, J. & Tønnesen, J.F.
5 1598 2017: Subaqueous rock-avalanche deposits exposed by post-glacial isostatic
6 1599 rebound, Innfjorddalen, Western Norway. *Geomorphology* 289, 117-133.
- 7 1600 Seppä, H., Bjune, A.E., Telford, R.J., Birks, H.J.B. Birks & Veski, S. 2009: Last nine-
8 1601 thousand years of temperature variability in Northern Europe. *Climate Past* 5,
9 1602 523-535.
- 10 1603 Shakesby, R.A. 2014: Rockfall. In Matthews, J.A., Barrow, C.J., Boyd, D.S.,
11 1604 Caseldine, C.J., Ficken, K.J., Innes, J.L., Nortcliff, S., Owen, G., Pike, J.,
12 1605 Shakesby, R.A., Walsh, R.P.D. & Wheeler, D.A. (eds): *Encyclopedia of*
13 1606 *Environmental Change, Volume 3*, 939-940. SAGE, London.
- 14 1607 Shakesby, R.A., Matthews, J.A. & Owen, G. 2006: The Schmidt hammer as a
15 1608 relative-age dating tool and its potential for calibrated-age dating in Holocene
16 1609 glaciated environments. *Quaternary Science Reviews* 25, 2846-2867.
- 17 1610 Shakesby, R.A., Matthews, J.A., Karlén, W. & Los, S. 2011: The Schmidt hammer as
18 1611 a Holocene calibrated-age dating technique: testing the form of the R-value-
19 1612 age relationship and defining predicted errors. *The Holocene* 21, 615-628.
- 20 1613 Soldati, M., Corsini, A. & Pasuto, A. 2004: Landslides and climate change in the
21 1614 Italian Dolomites since the Late Glacial. *Catena* 55, 141-161.
- 22 1615 Stahl, T., Winkler, S., Quigley, M., Bebbington, M., Duffy, B. & Duke, D. 2013:
23 1616 Schmidt hammer exposure-age dating (SHD) of late Quaternary fluvial
24 1617 terraces in New Zealand. *Earth Surface Processes and Landforms* 38, 1838-
25 1618 1850.
- 26 1619 Stock, G.M. & Uhrhammer, R.A. 2010: Catastrophic rock avalanche 3600 BP from El
27 1620 Capitan, Yosemite Valley, California. *Earth Surface Processes and Landforms*
28 1621 35, 941-951.
- 29 1622 Stoffel, M. & Huggel, C. 2012: Effects of climate change on mass movements in
30 1623 mountain environments. *Progress in Physical Geography* 36, 421-439.
- 31 1624 StormTech 2012: *Tech Sheet 1: porosity of structural backfill*.
32 1625 [http://www.stormtech.com/download_files/pdf/techsheet1.pdf]
- 33 1626 Stroeven, A.P., Hättestrand, C., Kleman, J., Heyman, J., Fabel, D., Fredin, O.,
34 1627 Goodfellow, B.W., Harbor, J.M., Jansen, J.D., Olsen, L., Caffee, M.W., Fink,
35 1628 D., Lundqvist, J., Rosqvist, G.C., Strömberg, B. & Jansson, K.N. 2016:
36 1629 Deglaciation of Fennoscandia. *Quaternary Science Reviews* 147, 91-121.
- 37 1630 Tomkins, M.D., Dortch, J.M., & Hughes, P.D. 2016: Schmidt Hammer exposure
38 1631 dating (SHED): Establishment and implications for the retreat of the last
39 1632 British Ice Sheet. *Quaternary Geochronology* 33, 46-60.
- 40 1633 Tomkins, M.D., Huck, J.J., Dortch, J.M., Hughes, P.D., Kirkbride, M.P. & Barr, I.D.
41 1634 2018a: Schmidt hammer exposure dating (SHED): calibration procedures, new
42 1635 exposure age data and an online calculator. *Quaternary Geochronology* 44,
43 1636 55-62.
- 44 1637 Tomkins, M.D., Dortch, J.M., Hughes, P.D., Huck, J.J., Stimson, A.G., Delmas, M.,
45 1638 Calvet, M. & Pallàs, R. 2018b: Schmidt hammer exposure dating (SHED):
46 1639 rapid age assessment of glacial landforms in the Pyrenees. *Quaternary*
47 1640 *Research* (in press).
- 48 1641 Tomkins, M.D., Dortch, J.M., Hughes, P.D., Huck, J.J., Tonkin, T., & Barr, I.D.
49 1642 2018c: Timing of glacial retreat in the Wicklow Mountains, Ireland,
50 1643 conditioned by glacier size and topography. *Journal of Quaternary Science* (in
51 1644 press).

- 1
2
3 1645 Torrence, C., & Compo, G.P. 1998: A Practical Guide to Wavelet Analysis. *Bulletin*
4 1646 *of the American Meteorological Society* 79, 61-78
- 5 1647 Trauth, M.H., Alonso, R.A., Haselton, K.R., Hermanns, R.L. & Strecker, M.R. 2000: Climate
6 1648 change and mass movements in the NW Argentine Andes. *Earth and Planetary*
7 1649 *Science Letters* 179, 243-256.
- 8 1650 Trauth, M.H., Bookhagen, B., Marwan, N. & Strecker, M.R. 2003. Multiple landslide
9 1651 clusters record Quaternary climate changes in the northwestern Argentine
10 1652 Andes. *Palaeogeography, Palaeoclimatology, Palaeoecology* 194, 109-121.
- 11 1653 Väiliranta, M., Salonen, J.S., Heikkilä, M., Amon, L., Helmens, K., Klimaschewski,
12 1654 A., Kuhry, P., Kultti, S., Paska, A., Shala, S., Veski, S. & Birks, H.H. 2015:
13 1655 Plant macrofossil evidence for an early onset of the Holocene summer thermal
14 1656 maximum in northernmost Europe. *Nature Communications*
15 1657 doi:10.1038/ncomms7809.
- 16 1658 Velle, G., Bjune, A.E., Larsen, J & Birks, H.J.B. 2010: Holocene climate and
17 1659 environmental history of Brurskardstjørne, a lake in the catchment of Øvre
18 1660 Heimdalsvatnet, south-central Norway. *Hydrobiologia* 642, 13–34.
- 19 1661 Viles, H., Goudie, A., Grabb, S. & Lalley, J. 2011: The use of the Schmidt hammer
20 1662 and Equotip for rock hardness assessment in geomorphology and heritage
21 1663 science: a comparative analysis. *Earth Surface Processes and Landforms* 36,
22 1664 320-333.
- 23 1665 Walker, M.J.C., Berkelhammer, M., Björk, S., Cwynar, L.C., Fisher, D.A., Long,
24 1666 A.J., Lowe, J.J., Newnham, R.M., Rasmussen, S.O. & Weiss, H. 2012: Formal
25 1667 subdivision of the Holocene Series/Epoch: a discussion paper by a Working
26 1668 Group of INTIMATE (Integration of ice-core, marine and terrestrial records)
27 1669 and the Subcommittee on Quaternary Stratigraphy (International
28 1670 Commission on Stratigraphy). *Journal of Quaternary Science* 27, 649-659.
- 29 1671 Wanner, H., Solomina, O., Grosjean, M., Ritz, S. & Jetel, M. 2011: Structure and
30 1672 origin of Holocene cold events. *Quaternary Science Reviews* 30, 3109-3123.
- 31 1673 Wilson, P. 2009: Storurdi: a late Holocene rock-slope failure (Sturzstrom) in the
32 1674 Jotunheimen, southern Norway. *Geografiska Annaler Series A Physical*
33 1675 *Geography* 91, 47-58.
- 34 1676 Wilson, P. & Matthews, J.A. 2016: Age assessment and implications of late
35 1677 Quaternary periglacial and paraglacial landforms on Muckish Mountain,
36 1678 northwest Ireland, based on Schmidt-hammer exposure-age dating (SHD).
37 1679 *Geomorphology* 270, 134-144.
- 38 1680 Wilson, P., Matthews, J.A. & Mourne, R.W. 2017: Relict blockstreams at Insteheia,
39 1681 Valldalen-Tafjorden, southern Norway: their nature and Schmidt-hammer
40 1682 exposure age. *Permafrost and Periglacial Processes* 28: 286-297.
- 41 1683 Winkler, S. 2009: First attempt to combine terrestrial cosmogenic nuclide (¹⁰Be) and
42 1684 Schmidt hammer relative-age dating: Strauchon Glacier, Southern Alps, New
43 1685 Zealand. *Central European Journal of Geosciences* 1, 274-290.
- 44 1686 Winkler, S. & Matthews, J.A. 2010: Holocene glacial chronologies: are 'high
45 1687 resolution' global and interhemispherical comparisons possible? *The Holocene*
46 1688 20, 1137-1147.
- 47 1689 Winkler, S. & Matthews, J.A. 2014: Comparison of electronic and mechanical
48 1690 Schmidt hammers in the context of exposure-age dating: are Q- and R-values
49 1691 interconvertible? *Earth Surface Processes and Landforms* 39, 1128-1136.
- 50 1692 Winkler S. & Matthews, J.A. 2016: Inappropriate instrument calibration for Schmidt-
51 1693 hammer exposure-age dating (SHD) – A comment on Dortch et al.,
52 1694 *Quaternary Geochronology* 35 (2016), 67-68. *Quaternary Geochronology* 36,

- 1
2
3 1695 102-103.
4 1696 Winkler, S., Chinn, T., Gärtner-Roer, I., Nussbaumer, U., Zemp, M. & Zumbühl, H.J.
5 1697 2010: An introduction to mountain glaciers as climatic indicators with spatial
6 1698 and temporal diversity. *Erdkunde* 64, 97-118.
7 1699 Winkler, S., Matthews, J.A., Mourné, R.W. & Wilson, P. 2016: Schmidt-hammer
8 1700 exposure ages from periglacial patterned ground (sorted circles) in
9 1701 Jotunheimen, Norway, and their interpretive problems. *Geografiska Annaler*
10 1702 *Series A Physical Geography* 98, 265-285.
11 1703 Zerathe, S., Lebourg, T., Braucher, R. & Bourlès, D. 2014: Mid-Holocene cluster of
12 1704 large-scale landslides revealed in the Southwestern Alps by ³⁶Cl dating.
13 1705 Insight on an Alpine-scale landslide activity. *Quaternary Science Reviews* 90,
14 1706 106-127.
15 1707
16 1708
17 1709
18 1710
19 1711
20 1712
21 1713
22 1714
23 1715
24 1716
25 1717
26 1718
27 1719
28 1720
29 1721
30 1722
31 1723
32 1724
33 1725
34 1726
35 1727
36 1728
37 1729
38 1730
39 1731
40 1732
41 1733
42 1734
43 1735
44 1736
45 1737
46 1738
47 1739
48 1740
49 1741
50 1742
51 1743
52 1744
53
54
55
56
57
58
59
60

FIGURE CAPTIONS

1745

1746

1747

1748

1749

1750

1751

1752

1753

1754

1755

1756

1757

1758

1759

1760

1761

1762

1763

1764

1765

1766

1767

1768

1769

1770

1771

1772

1773

1774

1775

1776

1777

1778

1779

1780

1781

1782

1783

1784

1785

1786

1787

1788

1789

1790

1791

1792

1793

1794

Fig. 1. Location map: numbers and open circles identify the studied SRSFs; sites of control points are shown by crosses.

Fig. 2. Photographs of selected small rock-slope failures (SRSFs): (A) No. 23, Gravdalen; (B) Nos 7 and 8, Leirdalen; (C) Nos 34-36, Bjørndalen; (D) No. 7, Sognefjell; (E) and (F) No. 22, Gravdalen (also the site of a young control point).

Fig. 3. Schematic of the fan-scar-cliff comparison tests with expected differences in mean R-values between fan boulders, scar bedrock surfaces, unfailed cliffs, and rock surfaces used as younger and older control-point surfaces. Expectations apply to single-event SRSF events without the possible complications discussed in the text.

Fig. 4. Frequency distributions of four SRSF characteristics: (A) fan volume; (B) altitude; (C) aspect; (D) mean R-value. Eight sites in gabbroic gneiss (Sognefjell) are differentiated by solid black shading from 84 sites in pyroxene-granulite gneiss.

Fig. 5. Calibration curves and calibration equations for (A) pyroxene-granulite gneiss and (B) gabbroic gneiss. Note that both calibration curves are based on two control points of known age (25 years and 9700 years) using data presented in Table 3.

Fig. 6. Holocene SHD chronologies of SRSF activity for Jotunheimen: (A) individual SHD dates with their 95% confidence intervals in the different subregions; (B) age-frequency distributions of SRSF events at the regional level using 2000-yr, 1000-yr, 500-yr and 200-yr time intervals; (C) weighted age-frequency distribution with age-frequency curve defined by binomial smoothing; (D) variation in the magnitude of SRSF events based on rock volume using 200-year time intervals. Vertical bands (numbered) are the 4 modes in the weighted age-frequency distribution suggesting phases of enhanced regional SRSF activity.

Fig. 7. Probability density function analysis of SRSF activity for Jotunheimen: (A) histogram and KS density PDE; (B) individual Gaussian age distributions ($n = 5$), the sum of which integrates to the cumulative PDE with a model fit that is graphically indistinguishable from the PDE model. The number of ages listed for each Gaussian age distribution (#) exceeds the total number of SRSF events identified in Jotunheimen as some ages contribute to >1 Gaussian distribution; (C) peak Gaussian numerical ages and 1σ uncertainties for the five individual Gaussian age distributions plotted against the peak probability density (PPD). The PPD scales with the number and spatial clustering of individual ages. Reported RSF volumes are based on the sum of individual SRSF volumes (m^3) which comprise each Gaussian age distribution; (D) distribution of SRSF ages, sorted by oldest to youngest. The 42 SRSF events which account for the dominant mode at 4.50 ± 1.42 ka (within 1σ) are highlighted.

Fig. 8. Change detection and related analyses: (A) cumulative sum change detection graph showing positive (blue) and negative (orange) changes and statistically significant departures ($> 2\sigma$) from the background SRSF frequency; (B) modelled permafrost depth in Fennoscandia (5% porosity) from Kukkonen & Šafanda (2001), subdivided into five distinct phases; (C) results of discreet Meyer wavelet analysis, showing the lowest frequency decomposed signal (d_6).

1795

1796 *Fig. 9.* Models for different patterns and causes of Holocene variations in RSF
 1797 frequency and/or magnitude: (1) continuity-of-activity; (2) intermittent-earthquakes;
 1798 (3) deglaciation-close-tracking; (4) deglaciation-lagging; (5) cool/wet-climate-
 1799 response; and (6) the new thermally-driven permafrost-degradation model proposed in
 1800 this study for SRSFs in Jotunheimen. The subdivisions of the Holocene shown are
 1801 those proposed by Walker et al. (2012).

1802

1803 *Fig. 10.* Relationships between SRSF frequency in Jotunheimen and proxy climatic
 1804 records: (A) temporal variations in SRSF frequency from Fig. 6C; (B) pollen-based
 1805 reconstruction of annual air temperature for Northern Europe expressed as deviations
 1806 from the mean (Seppä et al., 2009); (C) mean summer air temperature deviations from
 1807 present in the Scandes Mountains based on pine tree-limit variations (Dahl and Nesje,
 1808 1996); (D) pollen-based July air temperature variations at Øvre Heimdalsvatnet,
 1809 eastern Jotunheimen (Velle et al., 2010); (E) periods of above average air temperature
 1810 (shaded) based on the GISP 2 Greenland ice core $\delta^{18}\text{O}$ record (Alley, 2004; Wanner et
 1811 al., 2011); (F) periods of above average sea-surface temperatures in the North Atlantic
 1812 Ocean (shaded) based on standardized stacked ice-rafted debris (IRD) records (Bond
 1813 et al., 2001; Wanner, et al., 2011); (G) periods when glaciers in the Smørstabbtindan
 1814 massif, Jotunheimen, were smaller than today (shaded) based on glaciolacustrine and
 1815 glaciofluvial stratigraphy (Matthews and Dresser, 2008). Vertical bands indicate
 1816 phases of enhanced regional SRSF frequency (as in Fig. 6).

1817

1818

1819

1820

1821

1822

1823

SUPPLEMENTARY MATERIAL

1824

(Caption to be included with figure)

1825

1826

1827 Supplementary Fig. 1: Full results of discrete Meyer wavelet analysis, showing all six
 1828 decomposed signals (green), ranging from high (d_1) to low frequency (d_6), of which
 1829 the latter represents the only single event structure of Holocene SRSF activity. The
 1830 blue curves ($a_1 - a_5$) represent the cumulative aggregation of the decomposed signals
 1831 ($d_1 - d_6$) where a_6 represents the mean background rate of SRSF occurrence ($0.92 \pm$
 1832 0.20), which is identical to the Holocene mathematical mean. The sum of all
 1833 decomposed signals results in a model (S_m) that is identical to the 100 yr bin
 histogram data (S_d).

1834

1835

1836

1837

1838

1839

1840

1841

1842

1843

1844

1
2
3 1845 *Table 1.* Data on the 92 small rock-slope failures (SRSFs) located in Jotunheimen:
4 1846 Leirdalen (Nos 1-29); Bjørndalen (30-40); Gravdalen (41-68); Høgvaglura (69-72);
5 1847 Visdalen (73-80); Veodalen (81-84); Sognefjell (85-92).
6 1848 Abbreviations: L = fan length; W = fan width; V = fan volume; SD = standard
7 1849 deviation of R-values; C_s = error associated with the dated surface; C_c = error
8 1850 associated with the calibration equation; CI = confidence interval for the SHD age
9 1851 based on the total error (C_t).
10 1852

No.	L (m)	W (m)	V (m ³)	Altitude (m a.s.l.)	Aspect	Mean R-value	SD	C_s (yr)	C_c (yr)	SHD age (yr \pm 95% CI)	Sub-region
1	70	25	1050	1420	West	45.0	9.90	1047	513	7018 \pm 1124	Leirdalen
2	80	20	960	1440	West	44.51	8.80	930	414	7277 \pm 1018	
3	15	9	81	1400	West	39.69	9.47	1001	458	9833 \pm 1101	
4	90	40	2160	1160	West	41.53	9.57	1012	445	8857 \pm 1105	
5	15	8	72	1030	West	43.26	10.03	1060	426	7940 \pm 1143	
6	90	20	1080	1160	West	43.62	10.23	1081	423	7749 \pm 1161	
7	8	25	120	1140	West	44.69	9.41	995	412	7182 \pm 1077	
8	30	25	450	1140	West	46.59	10.35	1094	392	6175 \pm 1162	
9	8	8	38	1135	West	47.28	8.63	912	385	5809 \pm 990	
10	15	25	225	1135	West	44.68	8.85	936	412	7187 \pm 1022	
11	30	20	360	1200	North	52.38	10.07	1064	333	3105 \pm 1115	
12	50	25	750	1425	North	46.49	8.63	912	394	6228 \pm 994	
13	15	25	225	960	East	51.50	8.34	882	342	3572 \pm 946	
14	50	25	750	955	East	49.79	10.74	1135	360	4478 \pm 1191	
15	70	60	2520	950	East	49.28	8.73	923	365	4749 \pm 992	
16	50	25	750	1290	West	48.29	9.98	1055	375	5273 \pm 1120	
17	20	40	480	1320	West	54.10	9.90	1047	315	2193 \pm 1093	
18	20	15	180	1320	West	57.53	10.15	1073	280	375 \pm 1109	
19	30	40	720	1320	West	55.95	8.61	910	296	1213 \pm 957	
20	18	14	151	1120	East	48.79	8.43	891	370	5008 \pm 965	
21	16	8	77	1120	East	44.40	8.29	876	415	7336 \pm 970	
22	25	14	210	1130	East	48.93	9.11	963	368	4934 \pm 1031	
23	40	13	312	1170	East	41.30	9.14	966	447	8979 \pm 1065	
24	25	15	225	1180	East	40.82	9.16	968	296	9233 \pm 1012	
25	15	13	117	1180	East	43.37	9.49	1003	426	7882 \pm 1090	
26	20	4	48	1190	East	44.86	8.70	920	410	7092 \pm 1007	
27	12	8	58	1240	East	49.28	10.53	1113	365	4749 \pm 1171	
28	20	4	48	1240	East	45.92	10.98	1160	399	6530 \pm 1227	
29	22	4	53	1200	East	47.15	8.24	871	387	5878 \pm 953	
30	90	16	864	1370	East	44.27	10.65	1126	416	7405 \pm 1200	Bjørndalen
31	30	15	270	1380	East	44.62	10.10	1068	413	7219 \pm 1145	
32	30	10	180	1380	East	52.60	8.62	911	331	2989 \pm 922	
33	75	30	1350	1360	East	54.91	8.30	877	307	1764 \pm 930	
34	30	15	270	1380	East	49.87	7.53	796	359	4436 \pm 873	
35	30	12	216	1380	East	49.46	7.84	829	363	4653 \pm 905	
36	20	30	360	1380	East	50.19	8.61	910	355	4266 \pm 977	
37	80	35	1680	1330	South	50.23	9.57	960	355	4245 \pm 1024	
38	25	15	225	1300	North	54.07	6.73	711	316	2209 \pm 778	
39	50	30	900	1305	North	55.37	7.95	840	302	1520 \pm 893	
40	25	25	375	1300	North	53.30	8.20	867	323	2617 \pm 925	Gravdalen
41	55	20	660	1480	West	49.43	8.11	857	363	4669 \pm 931	
42	15	35	315	1480	West	55.49	6.69	707	301	1456 \pm 769	
43	65	15	585	1480	West	51.11	8.40	888	346	3778 \pm 953	
44	60	15	540	1470	West	50.84	7.05	745	349	3922 \pm 823	
45	65	25	975	1470	West	50.01	8.85	936	357	4362 \pm 1001	
46	30	15	270	1460	West	52.57	7.97	843	331	3004 \pm 905	
47	75	20	900	1460	West	53.03	6.27	663	326	2761 \pm 739	
48	25	30	450	1430	South	50.01	7.00	740	357	4362 \pm 822	
49	17	8	82	1440	South	49.10	8.45	893	367	4844 \pm 964	
50	40	15	360	1440	South	49.71	7.72	816	360	4521 \pm 892	
51	15	10	90	1440	South	50.38	7.78	822	356	4165 \pm 896	
52	15	6	54	1400	South	56.21	7.38	780	293	1075 \pm 834	
53	10	5	30	1400	South	57.99	6.22	658	275	131 \pm 713	
54	7	8	34	1360	South	47.32	8.00	846	385	5788 \pm 929	
55	10	6	36	1280	South	40.31	10.14	1072	457	9504 \pm 1165	
56	12	5	36	1440	South	48.82	8.12	858	370	4992 \pm 935	
57	6	5	18	1440	South	47.43	7.72	816	384	5729 \pm 902	
58	8	8	38	1440	South	51.63	7.70	814	341	3503 \pm 882	
59	4	5	12	1440	South	51.12	6.62	700	346	3773 \pm 781	
60	7	4	17	1480	South	48.02	7.43	785	378	5416 \pm 872	

61	20	5	60	1480	South	52.10	11.98	1266	336	3254 ± 1310	
62	14	8	67	1480	South	46.17	9.02	953	399	6397 ± 1033	
63	6	12	43	1430	South	48.74	8.09	855	370	5035 ± 932	
64	10	5	30	1430	South	46.99	7.65	809	388	5963 ± 897	
65	14	3	25	1460	South	49.91	8.38	886	358	4415 ± 956	
66	15	4	36	1520	South	51.92	8.34	882	338	3349 ± 944	
67	6	4	14	1540	South	49.95	9.74	1030	358	4393 ± 1090	
68	10	5	30	1540	South	49.37	7.08	748	364	4701 ± 832	
69	20	15	180	1550	East	50.13	7.74	818	356	4298 ± 892	Høgvaglura
70	50	12	360	1550	East	45.16	10.05	1062	407	6933 ± 1138	
71	20	10	120	1540	East	46.35	8.94	945	395	6302 ± 1024	
72	20	10	120	1540	East	42.10	11.92	1260	439	8555 ± 1334	
73	15	4	36	1420	East	47.03	11.08	1171	388	5941 ± 1234	Visdalen
74	15	9	81	1420	East	50.70	10.47	1107	350	3996 ± 1161	
75	10	4	24	1420	East	54.42	9.47	1001	312	2024 ± 1049	
76	25	10	150	1260	West	49.96	10.20	1078	358	4388 ± 1136	
77	40	20	480	1200	East	51.37	10.30	1089	343	3641 ± 1142	
78	70	30	1260	1200	East	52.98	8.86	937	327	2787 ± 992	
79	35	20	420	1200	East	51.57	7.93	838	341	3535 ± 905	
80	60	8	288	1190	East	50.31	10.75	1136	354	4202 ± 1190	
81	55	40	1320	1350	South	53.33	8.72	922	323	2601 ± 977	Veodalen
82	45	12	324	1340	South	54.33	9.34	987	313	2071 ± 1036	
83	50	25	750	1330	South	51.56	10.15	1073	341	3540 ± 1126	
84	45	40	1080	1330	South	49.46	10.60	1121	363	4653 ± 1178	
85	6	10	36	1375	East	37.17	11.29	900	239	9412 ± 931	Sognefjell
86	7	5	21	1425	South	38.53	8.82	703	244	8868 ± 744	
87	6	6	22	1425	South	39.42	10.43	831	247	8513 ± 868	
88	10	5	30	1430	South	41.38	9.86	786	255	7729 ± 826	
89	6	5	18	1430	South	40.73	9.47	755	253	7989 ± 796	
90	16	10	96	1450	South	38.26	8.83	704	243	8976 ± 745	
91	9	5	27	1435	West	42.33	10.03	800	259	7349 ± 840	
92	10	7	42	1370	East	36.95	9.14	729	238	9500 ± 766	

- 1853
- 1854
- 1855
- 1856
- 1857
- 1858
- 1859
- 1860
- 1861
- 1862
- 1863
- 1864
- 1865
- 1866
- 1867
- 1868
- 1869
- 1870
- 1871
- 1872
- 1873
- 1874
- 1875
- 1876
- 1877
- 1878
- 1879
- 1880
- 1881
- 1882
- 1883
- 1884
- 1885
- 1886

1887 *Table 2. Radiocarbon age control for deglaciation in the study area.*

Location	Altitude (m. a.s.l.)	¹⁴ C age ± 1σ (years BP)	Calibrated age* (cal. years BP)	Reference
<i>Leirdalen/Bjørndalen</i>				
Lower Leirdalen	920	9089 ± 61	10426 – 10170 (94.8%)	Barnett et al. 2000
Bøverkinnhalsen	1020	8570 ± 60	9677 – 9475 (95.4%)	Nesje & Dahl 2001
Bjørndalen	1250	8760 ± 100	10066 – 9547 (77.1%)	Matthews et al. 2005
<i>Sognefjell</i>				
Nedre Hervavatnet	1287	8695 ± 75	9921 – 9530 (94.6%)	Hormes et al. 2009
Gjuvvatnet	1248	8885 ± 140	10247 – 9557 (95.4%)	Karlén & Matthews 1992

* Most probable range with probability in brackets

1906 *Table 3. Control point data: values used for calibration equations are indicated in bold. Abbreviations: Gneiss = pyroxene-granulite gneiss; Gabbro = gabbroic gneiss; Combined = data combined from two replicate sites; SD = standard deviation; CI = confidence interval; n = sample size.*

Control point	Geology	Type	Age (years)	Mean R-value	SD	95% CI	n
Gravdalen	Gneiss	SRSF	25	58.22	6.29	0.72	300
Gravdalen	Gneiss	Road cut	25	58.15	6.56	0.75	300
Gravdalen	Gneiss	Combined	25	58.19	6.42	0.52	600
Sognefjell	Gabbro	Road cut	25	60.65	7.26	0.83	300
Gravdalen	Gneiss	Bedrock	9700	39.71	4.80	1.25	60
Leirdalen	Gneiss	Bedrock	9700	40.19	4.69	1.22	60
SE Smørstabbtindan	Gneiss	Combined	9700	39.94	4.79	0.87	120
Leirbreen	Gabbro	Bedrock	9700	35.78	2.84	0.74	60
Bøverbreen	Gabbro	Bedrock	9700	37.12	3.53	0.92	60
W Smørstabbtindan	Gabbro	Combined	9700	36.45	3.25	0.59	120

1913 *Table 4. Comparative R-values from fans, scars and unfailed cliffs associated with selected SRSFs. Further information on these six SRSFs are provided in Table 1.*

No.	Fan			Scar			Unfailed cliff		
	Mean	SD	95% CI	Mean	SD	95% CI	Mean	SD	95% CI
5	43.26	10.03	2.00	41.34	7.75	1.55	42.20	7.86	1.57
46	51.63	7.70	1.54	51.32#	8.10	1.62	41.63†	9.20	1.83
47	51.12	6.62	1.32	54.05#	8.05	1.69	43.26†	10.19	2.03
51	37.17*	11.29	2.25	42.89	9.73	1.94	38.54	10.37	2.07
58	36.95*	9.14	1.82	43.99	10.44	2.08	40.68	12.30	2.45
81	49.96*	10.20	2.03	54.47#	8.07	1.60	43.38†	10.78	2.15

* Fan significantly different from scar (p<0.05)

Scar significantly different from unfailed cliff (p<0.05)

† Unfailed cliff significantly different from fan (p<0.05)

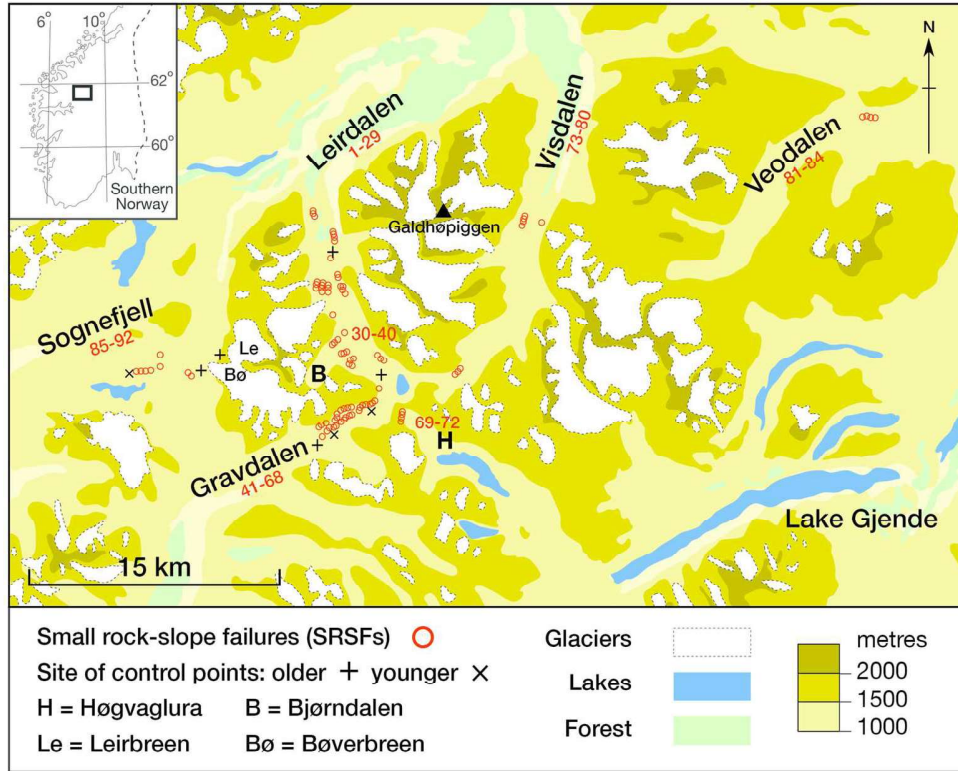


Fig. 1. Location map: numbers and open circles identify the studied SRSFs; sites of control points are shown by crosses.

143x115mm (300 x 300 DPI)

1
2
3
4
5
6
7
8
9
10
11
12
13
14
15
16
17
18
19
20
21
22
23
24
25
26
27
28
29
30
31
32
33
34
35
36
37
38
39
40
41
42
43
44
45
46
47
48
49
50
51
52
53
54
55
56
57
58
59
60

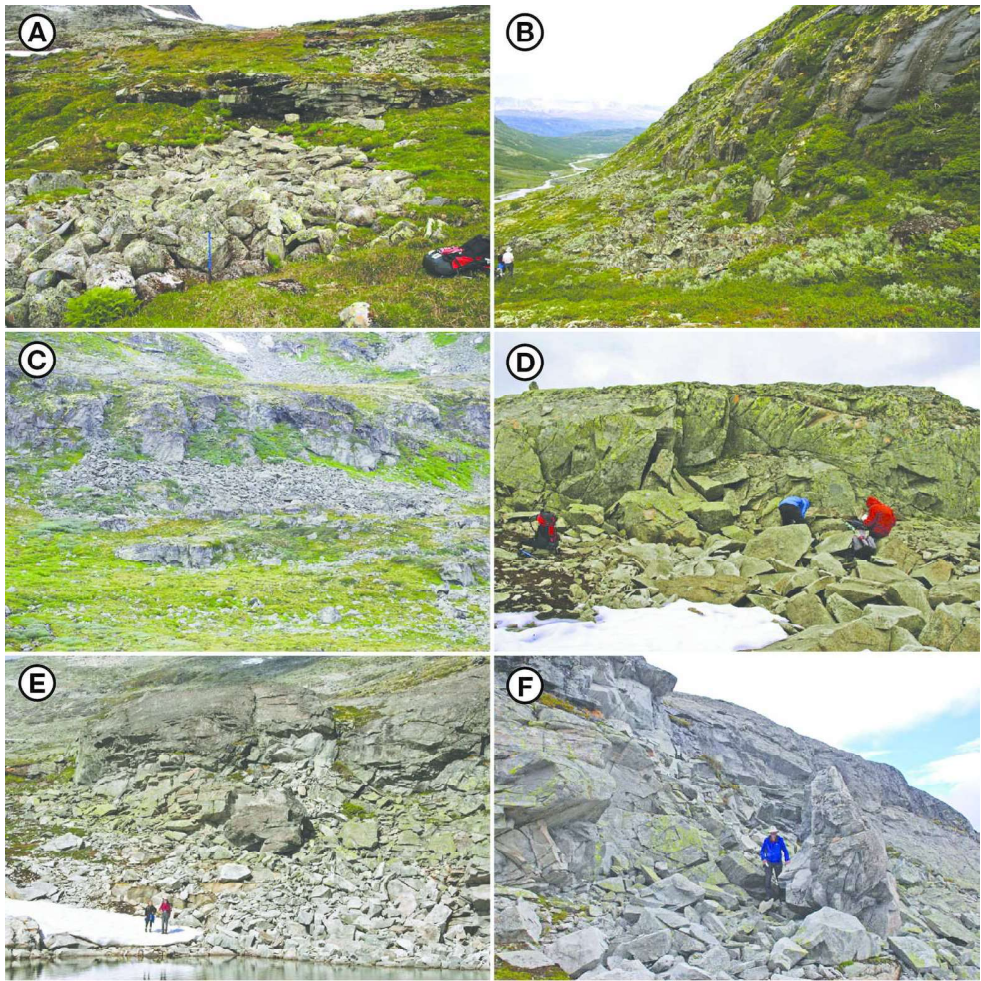
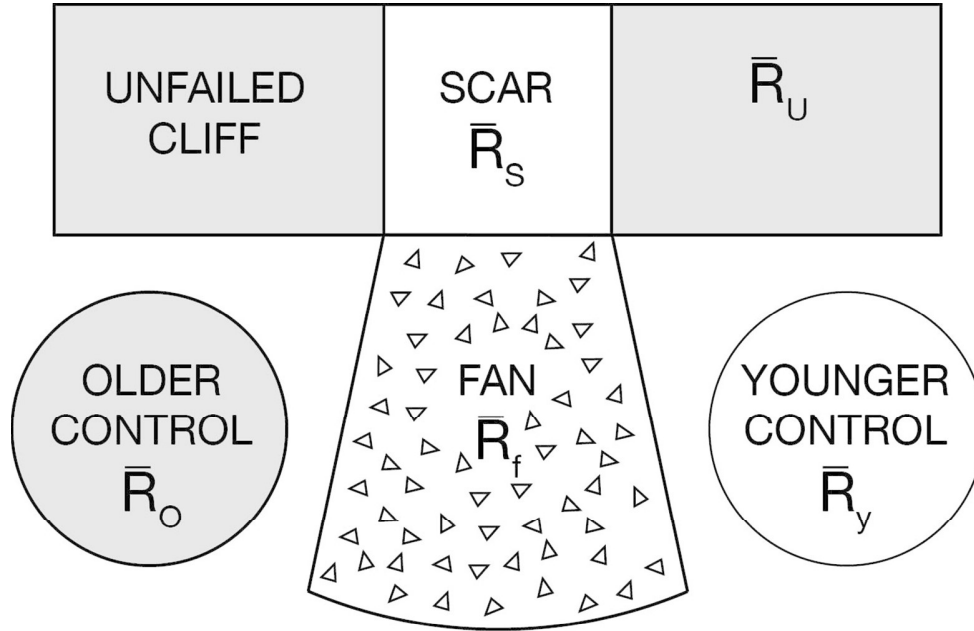


Fig. 2. Photographs of selected small rock-slope failures (SRSFs): (A) No. 23, Gravdalen; (B) Nos 7 and 8, Leirdalen; (C) Nos 34-36, Bjørndalen; (D) No. 7, Sognefjell; (E) and (F) No. 22, Gravdalen (also the site of a young control point).

174x173mm (300 x 300 DPI)



Expected mean R-values:

$$\bar{R}_y \geq \bar{R}_s = \bar{R}_f \geq \bar{R}_u \geq \bar{R}_o$$

Fig. 3. Schematic of the fan-scar-cliff comparison tests with expected differences in mean R-values between fan boulders, scar bedrock surfaces, unfailed cliffs, and rock surfaces used as younger and older control-point surfaces. Expectations apply to single-event SRSF events without the possible complications discussed in the text.

113x96mm (300 x 300 DPI)



1
2
3
4
5
6
7
8
9
10
11
12
13
14
15
16
17
18
19
20
21
22
23
24
25
26
27
28
29
30
31
32
33
34
35
36
37
38
39
40
41
42
43
44
45
46
47
48
49
50
51
52
53
54
55
56
57
58
59
60

1
2
3
4
5
6
7
8
9
10
11
12
13
14
15
16
17
18
19
20
21
22
23
24
25
26
27
28
29
30
31
32
33
34
35
36
37
38
39
40
41
42
43
44
45
46
47
48
49
50
51
52
53
54
55
56
57
58
59
60

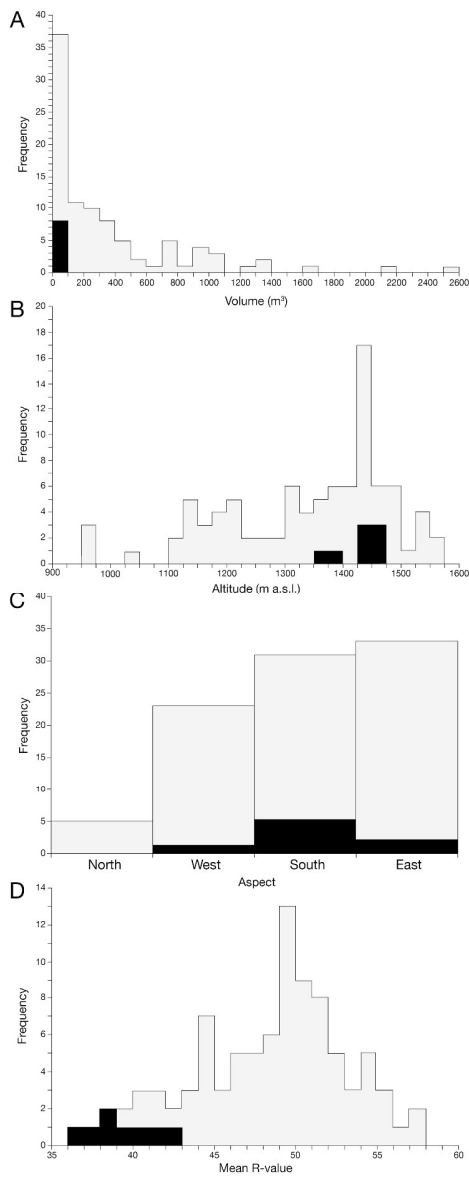


Fig. 4. Frequency distributions of four SRSF characteristics: (A) fan volume; (B) altitude; (C) aspect; (D) mean R-value. Eight sites in gabbroic gneiss (Sognefjell) are differentiated by solid black shading from 84 sites in pyroxene-granulite gneiss.

276x701mm (300 x 300 DPI)

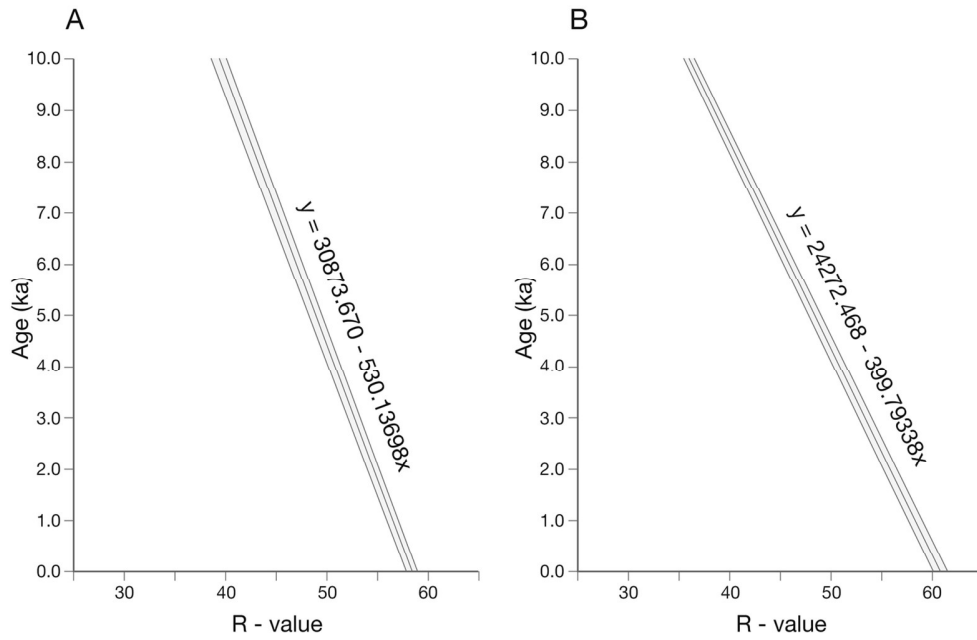


Fig. 5. Calibration curves and calibration equations for (A) pyroxene-granulite gneiss and (B) gabbroic gneiss. Note that both calibration curves are based on two control points of known age (25 years and 9700 years) using data presented in Table 3.

128x84mm (300 x 300 DPI)

View Only

1
2
3
4
5
6
7
8
9
10
11
12
13
14
15
16
17
18
19
20
21
22
23
24
25
26
27
28
29
30
31
32
33
34
35
36
37
38
39
40
41
42
43
44
45
46
47
48
49
50
51
52
53
54
55
56
57
58
59
60

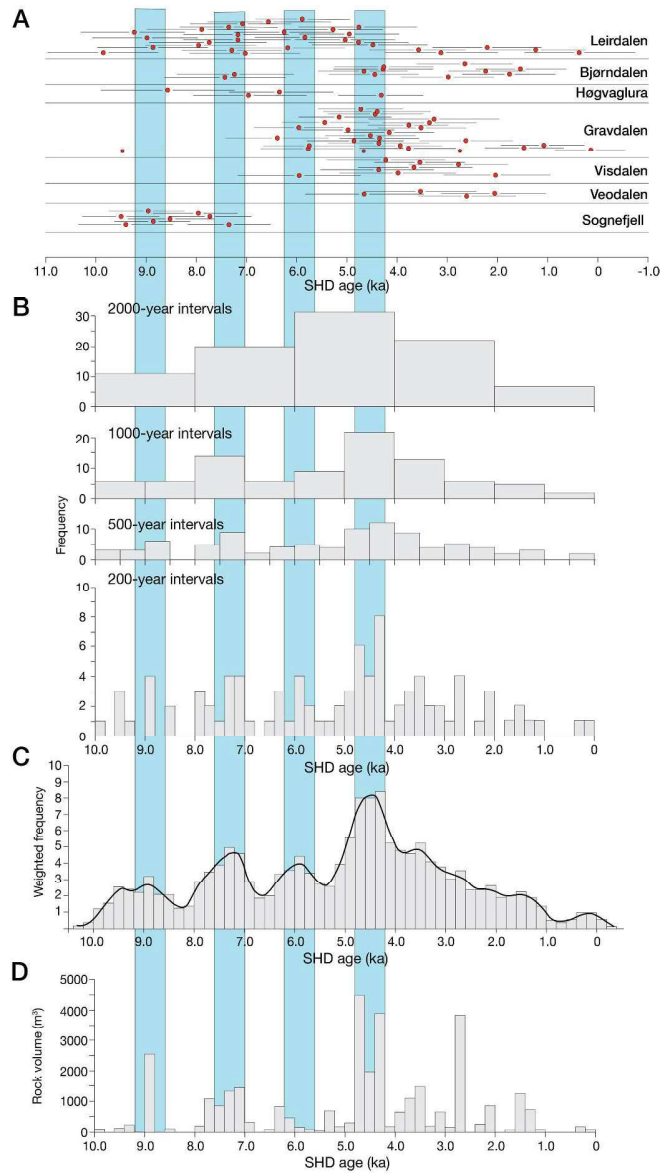


Fig. 6. Holocene SHD chronologies of SRSF activity for Jotunheimen: (A) individual SHD dates with their 95% confidence intervals in the different subregions; (B) age-frequency distributions of SRSF events at the regional level using 2000-yr, 1000-yr, 500-yr and 200-yr time intervals; (C) weighted age-frequency distribution with age-frequency curve defined by binomial smoothing; (D) variation in the magnitude of SRSF events based on rock volume using 200-year time intervals. Vertical bands (numbered) are the 4 modes in the weighted age-frequency distribution suggesting phases of enhanced regional SRSF activity.

332x598mm (300 x 300 DPI)

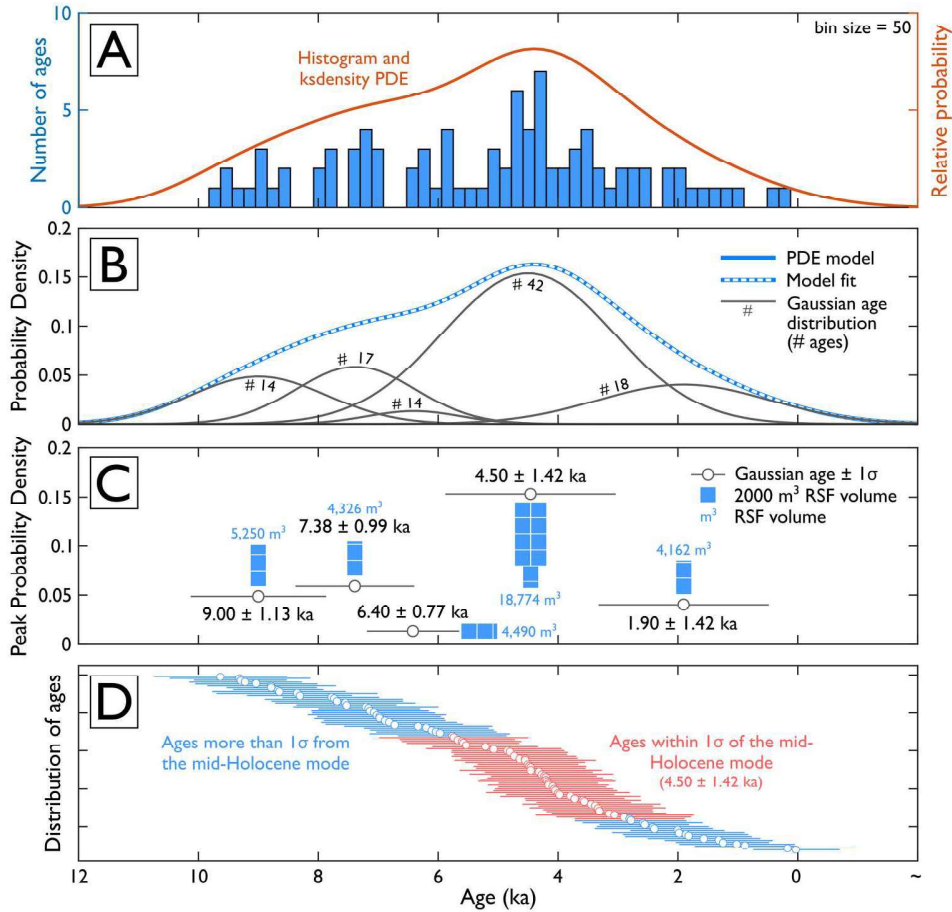


Fig. 7. Probability density function analysis of SRSF activity for Jotunheimen: (A) histogram and KS density PDE; (B) individual Gaussian age distributions ($n = 5$), the sum of which integrates to the cumulative PDE with a model fit that is graphically indistinguishable from the PDE model. The number of ages listed for each Gaussian age distribution (#) exceeds the total number of SRSF events identified in Jotunheimen as some ages contribute to >1 Gaussian distribution; (C) peak Gaussian numerical ages and 1σ uncertainties for the five individual Gaussian age distributions plotted against the peak probability density (PPD). The PPD scales with the number and spatial clustering of individual ages. Reported RSF volumes are based on the sum of individual SRSF volumes (m^3) which comprise each Gaussian age distribution; (D) distribution of SRSF ages, sorted by oldest to youngest. The 42 SRSF events which account for the dominant mode at 4.50 ± 1.42 ka (within 1σ) are highlighted.

190x180mm (300 x 300 DPI)

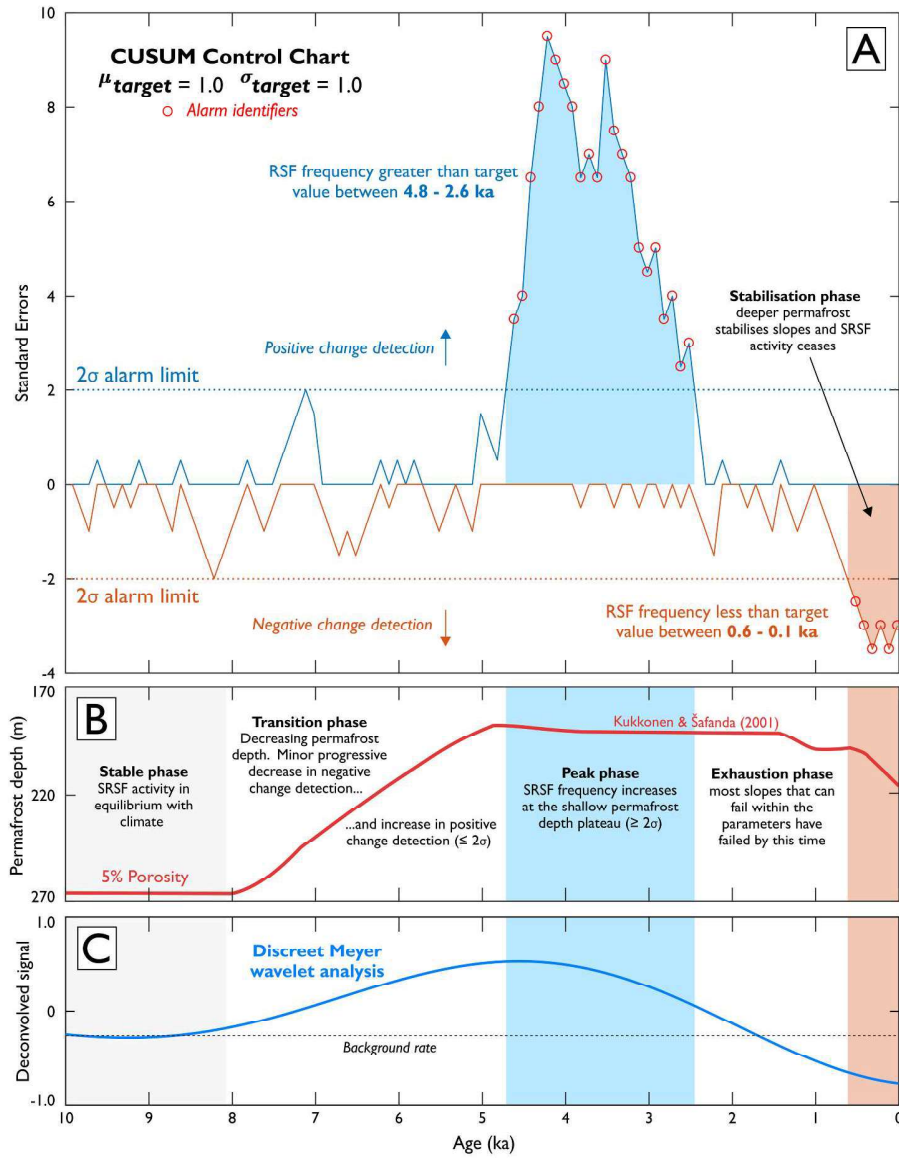


Fig. 8. Change detection and related analyses: (A) cumulative sum change detection graph showing positive (blue) and negative (orange) changes and statistically significant departures ($> 2\sigma$) from the background SRSF frequency; (B) modelled permafrost depth in Fennoscandia (5% porosity) from Kukkonen & Safanda (2001), subdivided into five distinct phases; (C) results of discrete Meyer wavelet analysis, showing the lowest frequency decomposed signal (d6).

293x372mm (300 x 300 DPI)

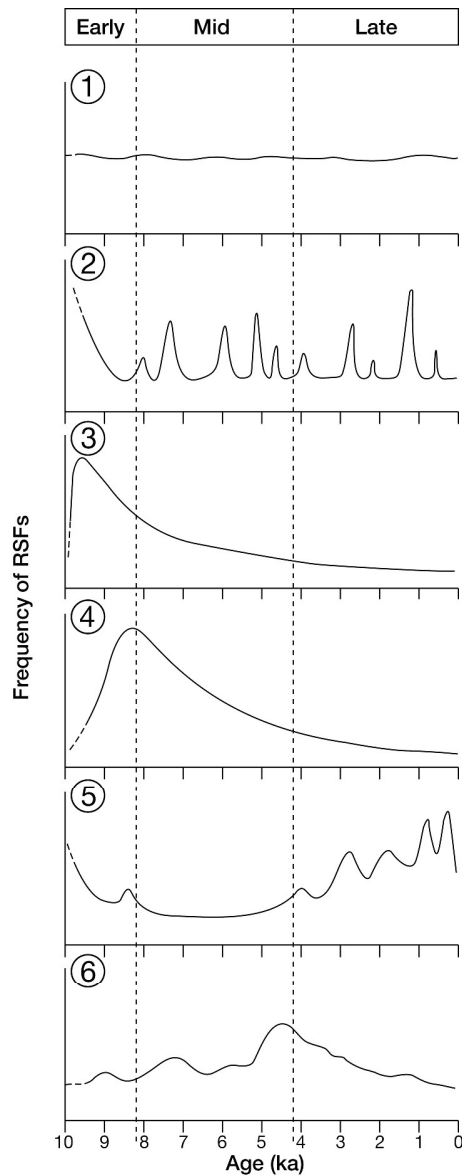


Fig. 9. Models for different patterns and causes of Holocene variations in RSF frequency and/or magnitude: (1) continuity-of-activity; (2) intermittent-earthquakes; (3) deglaciation-close-tracking; (4) deglaciation-lagging; (5) cool/wet-climate-response; and (6) the new thermally-driven permafrost-degradation model proposed in this study for SRSFs in Jotunheimen. The subdivisions of the Holocene shown are those proposed by Walker et al. (2012).

254x657mm (300 x 300 DPI)

1
2
3
4
5
6
7
8
9
10
11
12
13
14
15
16
17
18
19
20
21
22
23
24
25
26
27
28
29
30
31
32
33
34
35
36
37
38
39
40
41
42
43
44
45
46
47
48
49
50
51
52
53
54
55
56
57
58
59
60

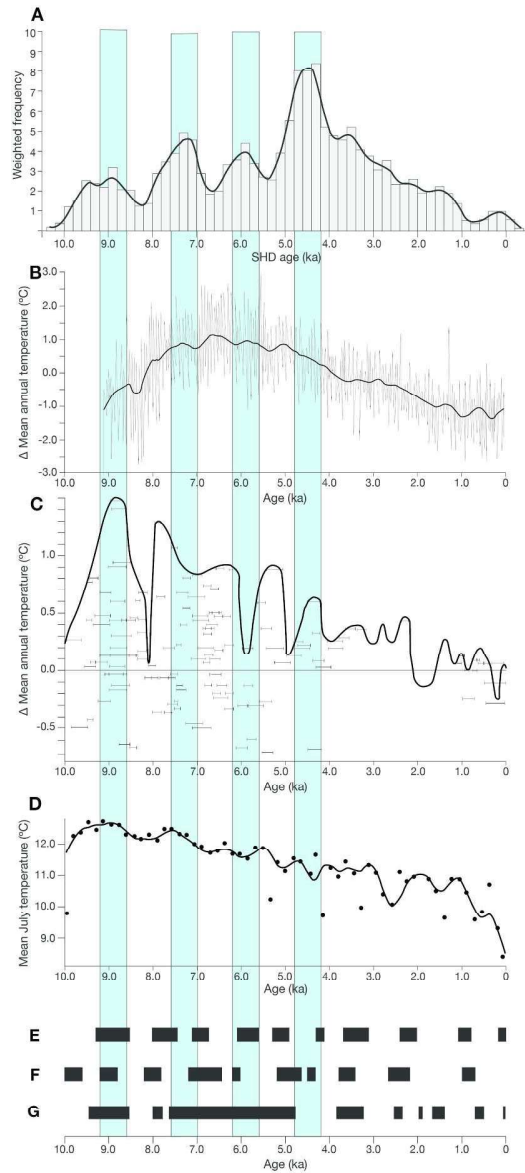


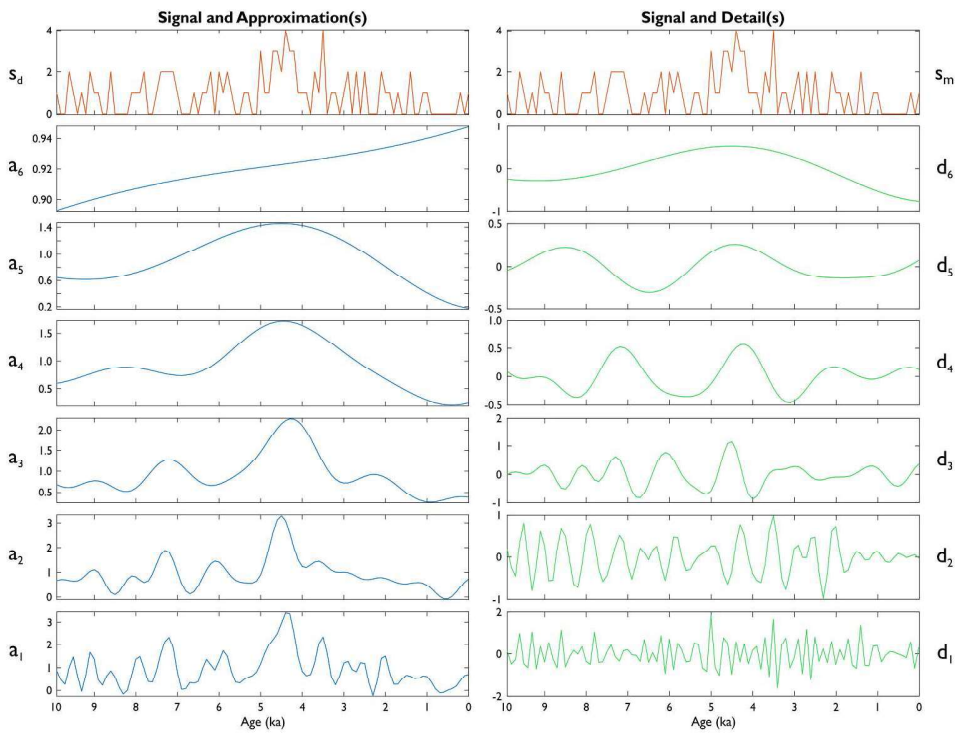
Fig. 10. Relationships between SRSF frequency in Jotunheimen and proxy climatic records: (A) temporal variations in SRSF frequency from Fig. 6C; (B) pollen-based reconstruction of annual air temperature for Northern Europe expressed as deviations from the mean (Seppä et al., 2009); (C) mean summer air temperature deviations from present in the Scandes Mountains based on pine tree-limit variations (Dahl and Nesje, 1996); (D) pollen-based July air temperature variations at Øvre Heimdalsvatnet, eastern Jotunheimen (Velle et al., 2010); (E) periods of above average air temperature (shaded) based on the GISP 2 Greenland ice core $\delta^{18}O$ record (Alley, 2004; Wanner et al., 2011); (F) periods of above average sea-surface temperatures in the North Atlantic Ocean (shaded) based on standardized stacked ice-rafted debris (IRD) records (Bond et al., 2001; Wanner, et al., 2011); (G) periods when glaciers in the Smørstabbtindan massif, Jotunheimen, were smaller than today (shaded) based on glaciolacustrine and glaciofluvial stratigraphy (Matthews and Dresser, 2008). Vertical bands indicate phases of enhanced regional SRSF frequency (as in Fig. 6).

272x612mm (300 x 300 DPI)

For Review Only

1
2
3
4
5
6
7
8
9
10
11
12
13
14
15
16
17
18
19
20
21
22
23
24
25
26
27
28
29
30
31
32
33
34
35
36
37
38
39
40
41
42
43
44
45
46
47
48
49
50
51
52
53
54
55
56
57
58
59
60

1
2
3
4
5
6
7
8
9
10
11
12
13
14
15
16
17
18
19
20
21
22
23
24
25
26
27
28
29
30
31
32
33
34
35
36
37
38
39
40
41
42
43
44
45
46
47
48
49
50
51
52
53
54
55
56
57
58
59
60



259x196mm (300 x 300 DPI)

Only